Universidade de São Paulo
Instituto de Astronomia, Geofísica e Ciências Atmosféricas
Departamento de Geofísica

Filipe Terra Nova dos Santos

Reversed flux patches on the archeomagnetic field

Lóbulos de fluxo reverso no campo arqueomagnético

São Paulo
2015

Filipe Terra Nova dos Santos

Reversed flux patches on the archeomagnetic field

Lóbulos de fluxo reverso no campo arqueomagnético

Submitted to the Instituto de Astronomia, Geofísica e Ciências Atmosféricas of Universidade de São Paulo for the degree of Master of Geophysics.

Department of Geophysics
Advisor: Prof. Dr. Ricardo Ivan Ferreira da Trindade

São Paulo
2015

to all that live in these four dimensions

Acknowledgements

I would like to thank all the support I got from my adivisor Prof. Ricardo Trindade. He was the same person who brought me into this inaccessible world - the core -, and who guided me through my academic career. To him I am extremely grateful. Here I also express my gratefulness to Dr. Gelvam Hartmann and Dr. Hagay Amit who counseled me enthusiastically and provided substantial help in my research. Both showed me exciting paths to unlock the core.

I would never be where I am with sanity without the help of my friend and geomagnetic colleague Wilbor Polleti, he always provided stimulus to my enthusiasm. I would not have the same joy working on Geomagnetism without the talks and laughs that Grasiane Mathias, Plinio Jaqueto, Giovanni Moreira, Danielle Brandt, Elder Yokoyama and Janine Araujo allowed me to share with them. I also thank all involved in the Lab of Paleomagnetism. They were all important in some way to me. That same lab one day will be called Lab of Geomagnetism and Core Dynamics (just an internal joke!).

Angelo Bianchi, Marta Aloy, Tatiana Karpischek and Lucas Diogo - I am happy as a clam because of you !. Every time I needed or I supposed that I needed support they were there. They are the beloved friends who I have the joy to share life with, and it has been such a pleasure. It is hard to imagine life without them. I will keep you always deep on my heart.

I also have special thanks to: Frederico Almeida who inspired me for his dedication and perseverance, I will never forget how he endured so much holding the biggest smile that I have ever seen. Marco Antonio who is such a joy to talk and be by his side. Uiran Silva who threw me through a window. João Estranho who pushed my limits in a good way. Thiago de Castro and Joao Zambrini to whom I could only say - you made the time

as good as it gets. I would like to make here a short and by far non exhaustive list of other people who made my days in this journey extremelly easy to deal with. You all are in my heart, even though sometimes it looks like I do not have one: Rui Omuro, Bruno Noronha, Rafael Bomfim, Hudson Lodi, Gabriela Muller, Ricardo Higa, Karine Carvas, Daniella Magalhães, Marcos Burn, Víctor Lellis, Tacio and Tulio Bicudo, Neils Wagner, Antonio Santos, Luara Lucas, Marcio Lima, Gabriel Moreira, Jessica Barabanov, Priscila Endo, Rogerio Sampaio, Pedro Sousa, Fernando Palhares, Camilla Sylos and many others.

I also want to cheer my beloved handball team (of course including coaches, ex coaches and ex athletes), which is one of the foundations of my life. It feels like family to me; the rock I can always stand on. Here I can't name no one, because as a team they are equally important, special to me in their crazy ways.

I thank all professors and employees of IAG-USP. They were always ready to help me whenever they could, and with a smile in the face. I also thank Fapesp, Santander, and CAPES for continuous support through scholarships along these years.

My family is everything I would dream to having, especially in our Christmas dinners. They are and will always be the most important thing to me. Even at distance I feel their support pushing me beyond my limits. Mother and Sister you rock!

At last I thank the inspiration, I wont name because it scares the hell out of me with punches and smiles. I just enjoy it.

"*I don't hate them...I just feel better when they're not around.*"

Charles Bukowski

"*Daring ideas are like chessmen moved forward. They may be beaten, but they may start a winning game*"

Johann Wolfgang von Goethe

Resumo

Modelos do campo arqueomagnético podem fornecer importantes informações sobre o geodínamo. Nesta dissertação, estudou-se a existência e a mobilidade de lóbulos de fluxo reverso (RFPs, em inglês) no campo arqueomagnético. Testes de robustez foram aplicados para diferentes modeles. Além disso, foram exploradas as relações entre RFPs e as variações do momento do dipolo axial (ADM, em inglês). Para tanto, foram desenvolvidos algoritmos topológicos para definir, identificar e mapear os RFPs em modelos do campo arqueomagnético (modelo CALS3k.4b e modelo GUFM1). O equador magnético foi usado para definir a polaridade ao invés do equador geográfico. Uma vez que cada ponto da grade de $1^\circ \times 1^\circ$ de latitude/longitude esteja associado com um hemisfério magnético e uma polaridade (normal ou reversa), o passo seguinte é identificar os picos de lóbulos de fluxo reverso. Para o passo final de identificação foi imposto um critério de intensidade para evitar pontos que possuem intensidade muito baixa. Para mapear lóbulos de fluxo reverso no tempo, foi codificado um algoritmo que calcula a distância de cada lóbulo para todos os lóbulos do próximo intervalo de tempo. Diferentemente das definições anteriores, lóbulos que residem no equador geográfico são adequadamente identificados com a nova definição de RFPs. A maioria dos RFPs exibe deriva para Oeste e mais de 75% deles migra em direção a altas latitudes. Ondulações do equador magnético e RFPs resultam de campo com momento oposto ao ADM. Modelos filtrados apresentam resultados de mapeamento semelhantes aos de modelos não-filtrados, e em alguns casos, surgem nos modelos filtrados novos RFPs. Resultados dos modelos CALS3k.4b e GUFM1 para o período de 1840 AD até 1990 AD mostram concordância para o mapeamento de lóbulos de fluxo reverso com maiores similaridades para os filtros mais fortes. Os resultados desta dissertação são compatíveis com a idéia que a advecção e a difusão de RFPs tem operado em conjunto causando o decréscimo do ADM nos últimos séculos. A ausência de RFPs no período de 550-1440 AD está relacionada a baixos valores nos graus intermediários do espectro de potência. Dessa forma, sugere-se que os RFPs são fortemente dependentes dos harmônicos esféricos de graus 4 e acima. Modelos filtrados e comparações com o modelo GUFM1 sugerem que lóbulos de fluxo reverso são feições robustas do campo magnético terrestre nos últimos milênios.

Abstract

Archeomagnetic field models may provide important insights into the geodynamo workings. Here I investigate the existence and mobility of reversed flux patches (RFPs) on the archeomagnetic field. In addition, the statistical behavior of RFPs, their robustness and the relations between RFPs and dipole changes were explored. Topological algorithms are introduced to define, identify and track RPFs in archeomagnetic field models. The magnetic equator was used to define RFPs, instead of the geographic equator. Once each point on the CMB grid is associated with a magnetic hemisphere and a polarity (normal or reversed), the next step is to identify the peaks of RFPs. For the final identification step a threshold criterion of intensity was imposed to avoid including insignificantly weak extreme points. To track RFPs in time, an algorithm was coded to calculate the distance of each RFP to all RFPs in the next snapshot. Model CALS3k.4b of Korte and Constable (2011) was applied for the interval 990 BC until 1990 AD, and both CALS3k.4b and GUFM1 models were applied for the interval between 1840 until 1990 AD. For both models on the CMB a grid of of 1° in longitude and latitude was applied on the CMB. Robustness tests were applied to the RFPs and results from models CALS3k.4b and GUFM1 were compared for the period 1840 to 1990 AD. In contrast to previous definitions, patches that reside on the geographic equator are adequately identified based on the new RFP definition presented here. Most RFPs exhibit a westward drift and 75% of them migrate towards higher latitudes. Undulations of the magnetic equator and RFPs oppose the axial dipole moment (ADM). Filtered models show a tracking behavior similar to non-filtered ones and new RFPs occasionally emerge. Results from CALS3k.4b and GUFM1 for the period 1840 to 1990 AD show a very good agreement between the tracking of RFPs in both field models. Stronger filters yield even more coincident RFPs positions and motions between the two models. As with CALS3k.4b, most RFPs in GUFM1 and their filtered models exhibit westward drift and migrate towards higher latitudes. Advection and diffusion of RFPs have worked in unison to yield the decrease of the ADM at recent times. The absence of RFPs in the period 550-1440 AD is related to a low in intermediate degrees of the geomagnetic power spectrum. I thus hypothesize that the RFPs are strongly dependent on intermediate spherical harmonic degrees 4 and above. Filtered models and comparison with GUFM1 suggest that RFPs are prominent features of the geomagnetic field over the past few centuries.

List of Figures

List of Tables

Contents

Chapter 1

Introduction

The geomagnetic field, generated by convective motions of an electrically conducting fluid in the Earth's outer core, is observed at the Earth's surface since about 1590 AD by ships, observatories and more recently at space by satellites (e.g. Jackson et al., 2000; Jonkers et al., 2003; Hulot et al., 2010). For periods before direct observations started the magnetic analysis of archaeological and geological materials (indirect observations) provide the information about the field. At first order, these two kinds of observations show that the field is dominated by an axial dipole. However, some non-dipole features are also present, particularly at the core-mantle boundary (CMB), in sectors where the polarity is opposite to that of the axial dipole (the so-called reversed flux patches, from hereafter RFPs). RFPs expansion and intensification over at least the past century contribute to the historical decrease in the intensity of the dipole moment (Gubbins, 1987).

Changes in the dipole are intrinsically related to changes of flow patterns at the top of the outer core, especially to core flow features near RFPs (Olson and Amit, 2006; Amit and Olson, 2008). Most of the radial field at the CMB is negative in the northern hemisphere and positive in the southern hemisphere. A normal flux patch has the same sign as its hemisphere, whereas an RFP has the opposite sign to its hemisphere. The most intense RFPs over the past decades are observed below the southern Atlantic hemisphere (e.g. Jackson et al., 2000; Olsen et al., 2010).

Direct measurements of the geomagnetic dipole intensity reveal a sustained rapid decrease since 1840 AD (Gubbins, 1987; Bloxham and Jackson, 1992; Jackson et al., 2000; Gubbins et al., 2006; Olson and Amit, 2006; Finlay, 2008). Dipole secular variation contributes substantially to the observed field variation at Earth's surface, in particular the steady decrease in dipole intensity over historical times. Therefore, its comprehension is

crucial to understand and perhaps predict how the field evolves. However, it is worth noting that at its source, the CMB, the dipolar fraction constitutes a very small part of the total secular variation; the secular variation spectrum is "blue", i.e. its power increases with harmonic degree being stronger at smaller scales. Hence, investigation of fluctuations in the geomagnetic dipole intensity must take into account the different contributions of the field to the axial dipole (Gubbins, 1987; Gubbins et al., 2006). In such analysis, the temporal variability in the integrated contribution of reversed flux to the axial dipole balances its total change (Olson and Amit, 2006). This emphasizes the role of RFPs in the decrease of the dipole intensity over the historical era. However, the role of RFPs in dipole changes over millennial timescales has not yet been explored.

Previous analyses of archeomagnetic field models were focused on the kinematics of high-latitude intense normal polarity flux patches. These patches were found to be mobile with alternating eastward-westward drifts (Dumberry and Finlay, 2007; Wardinski and Korte, 2008; Korte and Holme, 2010). Amit et al. (2010) designed an algorithm for identification and tracking of intense flux patches in numerical dynamos, and Amit et al. (2011) applied a similar algorithm for intense archeomagnetic flux patches. These high-latitude intense normal polarity flux patches and RFPs are thought to reflect distinctive dynamical mechanisms. Rapid rotation effects in the outer core result in a flow barrier, and surface convergence at the latitudes of the inner-core tangent cylinder (Aurnou et al., 2003). In an α^2 dynamo, columns of fluid that are nearly invariant in the direction of the rotation axis (Busse, 1970) intersect the CMB at these tangent cylinder latitudes (Olson et al., 1999). Downwelling associated with columnar cyclones (Olson et al., 2002; Amit et al., 2007) concentrate magnetic flux to produce the high-latitude intense patches (Olson and Christensen, 2002). The mobility of these field structures may be linked to the motion of the vortices (Amit et al., 2010), so their longevity may therefore maintain the axial dipole dominance. In contrast, low- and mid-latitude RFPs could be related to the expulsion of toroidal magnetic field by deep upwelling and radial diffusion below the CMB (Bloxham, 1986). If persistent, such local processes may eventually lead to a global polarity reversal (Aubert et al., 2008). Thus, the distinctive dynamo processes related to flux patches at differents latitudes motivate examining the time-dependence of RFPs, to compliment previous studies that described the mobility of high-latitude intense normal polarity flux patches (Dumberry and Finlay, 2007; Wardinski and Korte, 2008; Amit et al., 2011).

Here topological algorithms are developed to define, identify and track RFPs. They are applied to the CALS3k.4b archeomagnetic field model constructed for the past three millenia (Korte and Constable, 2011) and compared against the GUFM1 model for the interval between 1840 until 1990 AD. The robustness of the archeomagnetic RFPs is tested by using the historical field model GUFM1 (Jackson et al., 2000) to assess the reliability of the identification and tracking results.

An article reporting the main findings described in this dissertation is included as the Apendix A at the end of this volume. It appeared in Journal of Geophysical Research in January of 2015 under the title "The time dependence of archeomagnetic reversed flux patches", being authored by Filipe Terra-Nova, Hagay Amit, Gelvam A. Hartmann and Ricardo I.F. Trindade. As the senior author, I have conducted all analysis of the data, coded the algorithms and wrote the paper. Co-authors have helped with data interpretation, text revision and continuous discussions through the past two years.

Chapter 2

Dynamical origin of reversed flux patches

The purpose of this chapter is to summarize our current knowledge of the dynamical origin of reversed flux patches (RFPs). The physical meaning of RFPs is presented, as well as the fundamentals to describe them.

2.1 Secular Variation

The secular variation (SV) of the Earth's magnetic field comprises essentially the observed changes in the core-generated main field that occur on timescales of one year to thousands of years. It has much larger amplitude and lower frequency than changes associated with external electrical currents fluctuations, observed on timescales of seconds to days. The geomagnetic SV on the core-mantle boundary (CMB) is characterized by differents aspects in the past centuries, the most significant are: the westward drift (including, motion of large field features towards the west; Aubert et al. (2013)), hemispherical asymmetry (active Atlantic vs. quiet Pacific hemispheres; Holme et al. (2011)), axial dipole decay (the largest spatial scale of the field is persistently decreasing with time; Gubbins (1987)) and geomagnetic jerks (an abrupt change in the second time derivative of the geomagnetic field at Earth's surface; Courtillot and Mouel (1984)). These SV features may shed light on the dynamics in the outer core that generates the Earth's magnetic field.

2.2 Fundamentals

When an electrical conductor is pulled through a magnetic field, an electrical current is induced in the conductor. This current causes a magnetic field that adds to the original field such that the conductor appears to drag the field along with it. The combined magnetic

field interacts with the current resulting in a Lorentz force that acts on the conductor, opposing its motion. The relationship between magnetic field (B), electric field (E) and electrical current density (J) obeys Maxwell's equations:

$$\nabla \cdot E = \frac{\rho_e}{\epsilon_0} \tag{2.1}$$

$$\nabla \cdot B = 0 \tag{2.2}$$

$$\nabla \times E = -\frac{\partial B}{\partial t} \tag{2.3}$$

$$\nabla \times B = \mu_0 J + \epsilon_0 \mu_0 \frac{\partial E}{\partial t} \tag{2.4}$$

Note this is the form of Maxwell's equations for materials with no permanent magnetization or electric polarization and where ϵ_0 is the electrical permitivity of free space, μ_0 is the magnetic permeability of free space, ρ_e is the electric charge density and t is time. According to (2.2) there is no point of source/sink of magnetic field (i.e. no magnetic monopoles), therefore magnetic field lines are always closed, and the same number of field lines that enter must leave a volume.

The fluids in the outer core are moving electrical conductors, then the effective electric field in the frame moving with the conductor must be used, and the Ohm's law becomes

$$J = \sigma(E + u \times B) \tag{2.5}$$

where σ is the electrical conductivity.

Now, consider the relative magnitudes in (2.4) assuming that the magnetic field B has a characteristic magnitude $\mathcal{B}$, the electric field E has a characteristic magnitude $\mathcal{E}$, the lenghtscale of $\mathcal{L}$, and the timescale of τ:

$$\frac{|\epsilon_0 \mu_0 \frac{\partial E}{\partial t}|}{|\nabla \times B|} \sim \frac{\epsilon_0 \mu_0 \mathcal{E}/\tau}{\mathcal{B}/\mathcal{L}} \tag{2.6}$$

From a similar scale analysis of (2.3), $|\nabla \times E| \sim |-\partial B/\partial t|$ so that $\mathcal{E}/\mathcal{L} \sim \mathcal{B}/\tau$. Therefore:

$$\frac{|\epsilon_0 \mu_0 \frac{\partial E}{\partial t}|}{|\nabla \times B|} \sim \frac{1}{c^2} \frac{\mathcal{L}^2}{\tau} \tag{2.7}$$

Since the largest lenghtscales for the Earth's core is $\sim$ 3481 km and the shortest time

scale is $\sim$ 1 year the resultant of (2.7) is $\sim 10^{-19}$. Therefore, it is safe to neglect the displacement current term, since the balance of it and $\nabla \times B$ are significantly small.

2.3 Magnetic Reynolds number

The motion of an electrically conducting fluid in the outer core causes the secular variation of the Earth's magnetic field. The magnetic induction equation describes the electrodynamics of Earth's core. Being u the motion of the conductor and B the magnetic field, the field evolution in time is given by:.

$$\frac{\partial B}{\partial t} = \nabla \times (u \times B) + \eta \nabla^2 B \tag{2.8}$$

where $\eta = (\sigma \mu_0)^{-1}$. This equation arises from Maxwell's equations of electromagnetism and Ohm's law applied to moving conductors, under the magnetohydrodynamic approximation that motions are much slower than the speed of light. If the velocity field has a characteristic magnitude $\mathcal{U}$ and the magnetic field has a characteristic magnitude $\mathcal{B}$ and the lenghtscale over which both fields changes is $\mathcal{L}$, then the ratio of the magnitudes of the terms on the right hand side of 2.8 will be:

$$\frac{|\nabla \times (u \times B)|}{|\eta \nabla^2 B|} \sim \frac{\mathcal{U}\mathcal{B}/\mathcal{L}}{\eta \mathcal{B}/\mathcal{L}^2} \sim \frac{\mathcal{U}\mathcal{L}}{\eta} = R_m \tag{2.9}$$

where R_m is the magnetic Reynolds number. The evolution of the magnetic field is a competition between electromagnetic induction $\nabla \times (u \times B)$ and ohmic diffusion $\eta \nabla B^2$. The relative importance of these effects is quantified by the magnetic Reynolds number (Roberts, 2007). It can also be written as the ratio

$$R_m = \frac{\tau_\eta}{\tau_u} = \frac{\mathcal{L}^2/\eta}{\mathcal{L}/\mathcal{U}} \tag{2.10}$$

of the 'magnetic diffusion time' τ_η and the 'fluid advection time' τ_u. For a scale $\mathcal{L}$ corresponding to the Earth's outer core thickness and a value of $\eta = 0.7\ m^2 s^{-1}$ (Pozzo et al., 2012) then $\tau_\eta = 2 \times 10^5$ years, which is the time to the current system to decay in the absence of fluid flow. But the Earth is known to have possessed a field for at least 3.4×10^9 years (Kono and Tanaka, 1995). This implies that the Earth's magnetic field needs an

agent to balance the field destroyed by the $\eta\nabla^2 B$ term. According to the geodynamo hypothesis, this refers to the electromagnetic induction created by the term $\nabla \times (u \times B)$, and requires that the advection term creates new flux as rapidly as, or more rapidly than it is destroyed by magnetic diffusion. An estimate of $R_m \sim 1000$ is then provided using $\mathcal{L} = 2200\ Km, \mathcal{U} = 5 \times 10^{-4}\ ms^{-1}$ and $\eta = 1\ m^2 s^{-1}$, where the estimate of U comes from observing the speed of moving magnetic field structures (basically the westward drift).

2.4 The frozen flux approximation

Whilst the ohmic diffusion of magnetic fields in the core has a timescale of tens of thousands of years, the secular variation takes place on a shorter timescale. Roberts and Scott (1965) proposed that the magnetic flux is frozen into the core fluid as the core is treated as a perfect conductor over these timescales (i.e. fluid elements lying on a field line at some instant must continue to lie on the fluid elements at all later times). This is the 'frozen flux approximation'. Indeed, the Earth's core has $R_m >> 1$ which implies that the field generation is much stronger than ohmic dissipation. In the case of $R_m = \infty$, the second term on the right hand side of (2.8) is negligible (i.e. perfect conductivity), then

$$\frac{\partial B}{\partial t} = \nabla \times (u \times B) \tag{2.11}$$

By vector calculus relation

$$\nabla \times (u \times B) = (B.\nabla)u - (u.\nabla)B + u(\nabla.B) + B(\nabla.u)$$

and since the electrically conducting fluid is incompressible ($\nabla.u = 0$) and the magnetic field has no monopole ($\nabla.B = 0$), the following expression appears:

$$\frac{\partial B}{\partial t} = \nabla \times (u \times B) = (B.\nabla)u - (u.\nabla)B \tag{2.12}$$

where $(B.\nabla)u$ represents stretching of magnetic field by flow and $(u.\nabla)B$ represents advection of the magnetic field along with the flow. In the frozen flux approximation, the radial flux must be conserved through patches on the core-mantle boundary (CMB) bounded by curves of zero radial field (null-flux curves) (Backus, 1968). In this cenario, the

flow sweeps the magnetic field along with it, moving and stretching it, but never cuts or merges radial field lines, because magnetic diffusion is responsible to make magnetic field structures bounded by null-flux curves to merge/split as well as decay. The splitting of a null-flux curve into two curves is not a strong constraint because only a very small amount of dissipation is be required to complete the break (Gubbins and Bloxham, 1986). The same remark applies to the merging of two curves. It is important to emphasize that the main argument in favour of the frozen flux hypothesis has been the estimate of a large value of ~ 1000 for R_m in the outer. But this value of R_m may not be valid, for example, at the top of the core where shorter radial lenghtscales prevail due to the presence of a hydromagnetic boundary layer, resulting in strong effects of radial diffusion (Holme, 2007; Amit and Christensen, 2008).

2.5 Diffusion and Reversed Flux Patches

Gubbins and Bloxham (1986) used models of the main field at various epochs to find that while the frozen flux approximation appears to be valid over most of the CMB, the effects of diffusion are observed in a region centered under southern Africa and the south Atlantic Ocean, where features bounded by null-flux curves had reversed flux with respect to the axial dipole field of their hemisphere. Later Bloxham (1986) considered a simple 2-D kinematic model of convection to indicate that flux expulsion, through the action of diffusion on the field convected towards the boundary (upwelling motion of fluids acting on a strong toroidal field), is a viable mechanism and provides a simple explanation to these features. Futhermore if the initial toroidal field is strong, even if the diffusion of the toroidal field through the CMB is slow, the effect of these features on the poloidal field may be quite large (Bloxham, 1986). This process will have a much smaller lenghtscale due to the upwelling, then τ_η will be lower and diffusion effects could act in timescales similar to advection (Amit and Christensen, 2008).

Regions affected by diffusion bounded by a null-flux curve with a reversed flux to its hemisphere (see figure 2.1) are the so-called reversed flux patches (RFPs). These are small-scale features of the field, that need high resolution magnetic fields to precisely resolve them (see chapter 4). Intensification and poleward motion of RFPs can lead to a weaker axial dipole (see chapter 5, section 5.2 Dipole Changes). Indeed, some authors have proposed

that the proliferation of RFPs on the core-mantle boundary is a significant mechanism behind the rapid decrease in the dipole intensity over the historical period (Olson and Amit, 2006).

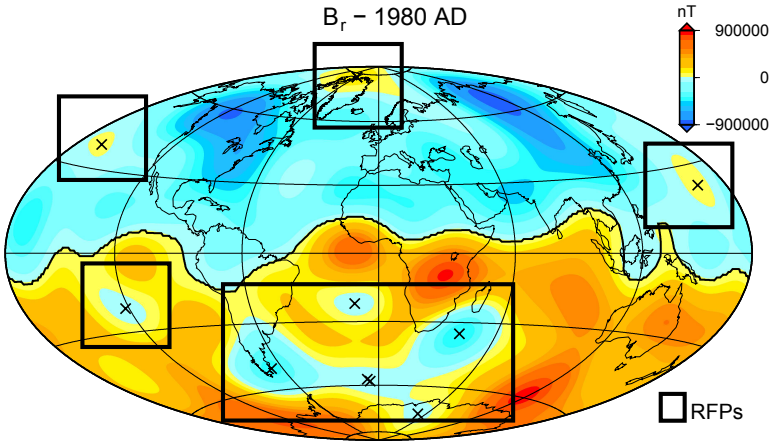

Figure 2.1: Radial geomagnetic field on the CMB at 1980 AD based on the CALS3k.4b archeomagnetic field model of (Korte and Constable, 2011). The black boxes mark identified RFPs. Note that while magnetic hemisphere north/south (determined by the magnetic equator instead the geographic equator) has negative/positive polarity, RFPs have the opposite polarity of its magnetic hemisphere.

This work will focus on the time-dependence of reversed flux patches and study the continuity of them. The main questions to be adressed are: "Are RFPs real small scale features of the field or are they just a consequence of noise in field models?"and "Are these features continuous in time at centennial timescales?". Backus (1988) alerted to this matter, when he argued that error estimates of Bloxham and Gubbins (1985a) and Gubbins and Bloxham (1986) were rather optimistic. The same also applies to Barraclough et al. (1989) when they found no evidence for frozen flux approximation violation, but admitted that field models used were not accurate enough to exclude the hypothesis. Jackson and Finlay (2007) remarked that the published and well accepted time-dependence field models of Bloxham and Jackson (1992) and Jackson et al. (2000) both show an obvious growth in the intensity of RFPs in the Southern hemisphere in the twentieth century. Yet, the available record of the field seem incapable of constraining field models sufficiently to ascertain that explusion of toroidal flux by upwelling core fluid is the mechanism behind this intensification of RFPs. It is generally acknowledged that the frozen flux approximation inevitably fails but it still provides useful information about fluid motions at the core surface and substantial parts of the secular variation pattern can be explained using it(Jackson and Finlay, 2007). In fact, errors in the field models due to oversimplified

dynamical assumptions and also to those related to the limits on the range of spherical harmonic coefficients can pose more serious problems to the inversion than the violation of the frozen flux approximation (Jackson and Finlay, 2007). So, it is clear that it is a major challenge to know if RFPs are robust features of the Earth's magnetic field or not.

Chapter 3

Methods

This chapter describes the methods for identification and tracking of reversed flux patches (RFPs), the algorithm to find peaks, and the filtering criteria used. The methodology to study dipole changes and the robustness tests are also presented. The codes for identification and tracking of RFPs are provided in Appendix B.

3.1 Identification and tracking of RFPs

RFPs are usually defined as positive/negative radial field structures in the northern/-southern hemispheres (e.g. Olson and Amit, 2006). But this definition might be problematic, particularly for low geographic latitudes. For example, a patch residing on the geographic equator is considered by this definition as partly normal partly reversed. Therefore, a more appropriate definition is needed. One way to solve this problem is by defining the RFPs using the magnetic equator instead of the geographic equator as the reference. An algorithm to map the magnetic equator was then developed, such that at a given longitude on the CMB, the magnetic equator is defined as the point where the radial geomagnetic field B_r changes sign. To distinguish between sign changes associated with the magnetic equator from sign changes related to an RFP, the algorithm searches first a longitude where there is only one point of change in the sign of B_r. This point is guaranteed to be the magnetic equator. From this initial location of the magnetic equator, the algorithm selects the closest point on the neighbor longitude which shows a change in sign of B_r and so on. After mapping the magnetic equator the magnetic hemispheres are defined. Then, every grid point north/south of the magnetic equator is assigned to its respective magnetic hemisphere. A difficulty arises at some longitudes where the magnetic

equator appears more than once. An algorithm marches from co-latitude 0° to 180°, assigning the northernmost point to the northern magnetic hemisphere. Then, after every time crossing of the magnetic equator, the next point is assigned to the opposite hemisphere.

Once each point on the CMB grid is associated with a magnetic hemisphere and a polarity (normal or reversed), the next step is to identify the peaks of RFPs. For this purpose an algorithm was coded to determine field maxima and minima of flux patches at the CMB. The algorithm searches the maxima and minima of the radial field by comparison with neighboring cells. A grid point is considered to be a maximum/minimum if it has a higher/lower value than its eight neighboring cells. Maximum or minimum values indicate the coordinates (co-latitude and longitude) of the peak of the RFPs at the CMB. For the final identification step a criterion of threshold intensity was imposed to avoid interpreting insignificantly weak extreme points as RFPs. For every time frame, only RFPs with peak values larger than half the most intense RFP of the same time frame were considered. Obviously, only snapshots with more than one RFP were affected by this criterion.

To track RFPs in time, an algorithm was coded to calculate the distance of each RFP to all RFPs in the next snapshot. The spherical distance is calculated along a great circle. A critical distance was set based on typical large-scale core flow values from geomagnetic secular variation inversions. In the core flow model of Amit and Olson (2006), the maximum time-average flow plus one standard deviation is about 70 km/yr. I used this value multiplied by the time step between snapshots of 10 yrs to obtain the critical distance for tracking. A pair of RFPs at two successive time frames which has a spherical distance lower than this critical value is considered to be the same RFP. If an RFP is farther than the critical distance from all RFPs from the previous time frame, it is denoted as a new RFP.

3.1.1 Dipole changes

The above definitions were then used to map local contributions to the axial dipole moment (ADM) and their temporal oscillations. The axial component of the magnetic dipole moment (m_z) is defined as follows (Moffatt, 1978; Gubbins, 1987; Gubbins et al., 2006; Olson and Amit, 2006):

$$m_z = \frac{4\pi a^3}{\mu_0} g_1^0 = \frac{3r_o}{2\mu_0} \int_S B_r cos\theta dS \tag{3.1}$$

where a is the radius of the Earth, $\mu_0 = 4\pi \times 10^7 Hm^{-1}$ is the free space magnetic permeability, g_1^0 is the axial dipole Gauss coefficient, r_o is the radius of the core, B_r is the radial component of the magnetic field on the CMB, θ is co-latitude and dS denotes a CMB surface increment. The integrand $B_r cos\theta$ represents the spatial distribution of local contributions to the ADM. Thus, mapping $B_r \cos\theta$ allows imaging local contributions to the ADM.

Different types of $B_r \cos\theta$ structures were associated to different ADM contributions as:

$$m_z = m_{n+} + m_{n-} + m_{r+} + m_{r-} \tag{3.2}$$

where subscripts n and r denote contributions from regions of normal and reversed flux respectively, m_{n+} represents reinforcing contributions (mostly from high latitude flux patches), m_{n-} corresponds to opposite contributions (from magnetic equator undulations), m_{r+} represents reinforcing contributions and m_{r-} denotes opposite contributions. Note that m_{r+} contributions appear when an RFP is localized at least partly between the magnetic equator and the geographic equator.

3.1.2 Robustness tests

Uncertainties in archeomagnetic field models will produce erroneous results concerning the existence and mobility of RFPs. Robustness tests were then performed, one using the power spectrum, the other using low pass filtered fields.

The Mauersberger-Lowes spectrum at the CMB is one of the primary outputs of the dynamo process in the core (Dormy et al., 2000). The magnetic field spectrum R_n at the CMB can be expressed as a function of spherical harmonic degree n in terms of the Gauss coefficients of the core field as (Lowes, 1974):

$$R_n = (n+1)\left(\frac{a}{r_o}\right)^{2n+4} \sum_{m=0}^{n} (g_n^m)^2 + (h_n^m)^2 \tag{3.3}$$

where n is degree, m is order, and the sets g_n^m and h_n^m are the Gauss coefficients. I compared the spectrum at periods without RFPs with the spectrum at periods with RFPs to test whether the absence of patches is due to low field resolution manifested by a steeper descending spectrum.

In the second test, I defined a low pass filter $F(n)$ by

$$F(n) = \begin{cases} 1 & \text{, if } n < n_0 \\ cos\left(\frac{n-n_0}{n_f-n_0} \cdot \frac{\pi}{2}\right) & \text{, if } n \geq n_0 \end{cases} \tag{3.4}$$

where n_0 marks the beginning of the filtering and n_f marks the truncation. At $n = n_f$ the filter $F(n_f) = 0$, so the highest degree considered is n_{f-1}. I examined the sensitivity of the identification and tracking of RFPs down to the small-scale field, which is most uncertain in the archeomagnetic field models, by comparing the original results using non-filtered model with those obtained using different low-pass filtered models. Finally the results were compared with those based on the historical field model GUFM1 (Jackson et al., 2000) that has much better temporal and spatial resolution to assess the robustness of the results from archeomagnetic models.

Chapter 4

Models

Global, spherical harmonic, field models are now routinely derived from satellite and observatory data. The most widely used model of the present geomagnetic field is the International Geomagnetic Reference Field (IGRF), but for archeomagnetic studies other models with appropriate time frames are required. In this chapter I firstly show the method used for spherical harmonic field models. Then, I present some archeomagnetic models, including a set of new models recently published and the historical field model GUFM1 (Jackson et al., 2000). Details of the models used in this work, emphasizing the data quality and distribution, and the errors associated to them are also shown.

4.1 Spherical harmonic field modelling methodology

The geomagnetic field is a vector field that can be represented by the field intensity B, the declination D between the geographic north and the horizontal component of the field and the inclination I between the field and the horizontal surface.

The geomagnetic field obeys Maxwell's equations (2.1 to 2.4). Combining Ampere's law at an insulator and the non-divergence of the field (equations 2.1 and 2.2), the Laplace equation is obtained for the magnetic potential V outside the dynamo generation region (e.g. Merrill et al., 1998). In spherical coordinates r (radial), θ (co-latitude) and λ (longitude), this equation is written as

$$\frac{1}{r^2}\left(\frac{\partial V}{\partial r}\left(r^2\frac{\partial V}{\partial r}\right)+\frac{1}{sin\theta}\frac{\partial}{\partial\theta}\left(sin\theta\frac{\partial V}{\partial\theta}\right)+\frac{1}{sin^2\theta}\frac{\partial^2 V}{\partial\lambda^2}\right)=0 \qquad (4.1)$$

The solution to the partial differential equation (4.1) is the well-known set of spherical harmonic functions:

$$V = a\sum_{n=0}^{\infty}\sum_{m=0}^{n}\left(\frac{a}{r}\right)^{n+1} P_n^m(cos\theta)(g_n^m cosm\lambda + h_n^m sinm\lambda) \tag{4.2}$$

where a is the radius of the Earth, P_n^m are the Schmidt semi-normalized Legendre polynomials, n is degree and m is order. The sets g_n^m and h_n^m are the Gauss coefficients which define the field model. For example, the coefficient g_1^0 represents the axial magnetic dipole, the coefficients g_1^1 and h_1^1 represent the equatorial dipole, the coefficients with $n = 2$ represent the quadrupole, etc. The Gauss coefficients are inverted from observations of the magnetic field. The strength of equation (4.2) is that given a set of Gauss coefficients the field can be downward continued to the CMB in a straightforward manner. Finally, considering $B = -\nabla V$ the orthogonal components of the geomagnetic field (North, East and Vertical, respectively) can be written in terms of the magnetic potential:

$$X = -B_\theta = \frac{1}{r}\frac{\partial V}{\partial \theta} \tag{4.3}$$

$$Y = -B_\lambda = \frac{1}{rsin\theta}\frac{\partial V}{\partial \lambda} \tag{4.4}$$

$$Z = -B_r = \frac{\partial V}{\partial r} \tag{4.5}$$

4.2 Overview of archeomagnetic models

The Earth's magnetic field can be represented by time-dependent field models. Large compilations of geomagnetic field observations are needed to derive such models. They are the basis for testing proposed mechanisms of field evolution (secular variation) and they underlie ongoing attempts to understand and predict future field behaviour (Finlay, 2008). At present the most widely used historical field is GUFM1 (Jackson et al., 2000). The recent published CALS3k.4 and CALS3k.4b field models (Korte and Constable, 2011) represent the last versions of the CALS3k models series. They have power spectrum values similar to the GUFM1 in lower degrees (Korte and Holme, 2010) but they fail to emulate it on higher degrees, therefore small scales of the field may be poorly represented by them (details will be explored in the next section).

Licht et al. (2013) introduced ensembles of time-varying archeomagnetic field models, consisting of a reference model, a mean model and a thousand individual models built from archeomagnetic, volcanic and sedimentary data sets, covering the past three millennia. These ensembles can be used to describe the field at any location from the core surface to the magnetosphere, and assess the way uncertainties due to the limited distribution and quality of the data affect any of its components or parameters, such as individual Gauss coefficients. They provide alternative descriptions of the archeomagnetic field to those provided by previously published archeomagnetic field models, where errors affecting the data, and errors due to non-modeled small spatial scales of the field, are taken into account explicitly. Unfortunately they limited their models to lower degrees. So, their models do not have enough resolution to study small-scale features of the Earth's magnetic field, but are good enough to see intense RFPs emerging.

Recently, Pavón-Carrasco et al. (2014) proposed a new archeomagntic field model based only on archeomagnetic and lava flow data, excluding lake sediment data. The model predictions agree with those of ARCH3k.1 (Korte et al., 2009) but it is not appropriate for global studies, due to lack of data from the Southern hemisphere. Pavón-Carrasco et al. (2014) models represents an improvement in field data resolution for times before 3000 years, but have lower resolution than the CALS3k series models for earlier times. Also recently, (Nilsson et al., 2014) presented a new family of spherical harmonic geomagnetic field models spanning the past 9000 years based on magnetic field directions and intensities obtained from archaeological artifacts, igneous rocks and sediments. Their new modelling strategy introduces alternative data treatments with a focus on extracting more information from sedimentary data. As a result of the data adjustments, power has been shifted from quadrupole and octupole to higher degrees compared with previous Holocene geomagnetic field models.

Each of these models addresses differents aspects of the archeomagnetic and historical fields. The GUFM1 was constructed with direct data, therefore it does not carry the errors from archeomagentic and sedimentary materials into its data set, which is the main concern in archeomagnetic field models. On the other hand, the time span of the GUFM1 is short for the archeomagnetic studies of RFPs. Models CALS3k.4 and CALS3k.4b were performed for the last 3000 years, are well resolved at higher degrees for recent times and are widely known as the best archeomagnetic model for global studies. Nevertheless,

they have been criticized on the data quality, mostly due to poorly global distribution and errors in dating of sediment records. Nonetheless these models have the best data distribution of all models presented here. They adopt an strategy that considering all the data available would provide more reliable models than filtering the data. The model of Pavón-Carrasco et al. (2014) was not yet widely used, its data set comes almost entirely from the Northern hemisphere, so it is not appropriated for global studies. The model of Licht et al. (2013) resolves intense RFPs, even though it is only appropriate to study larger features of the field, because the authors wanted to put their efforts on describing the SV in the surface for applications on geomagnetic data assimilation. The model of Nilsson et al. (2014) appears to be good to study RFPs since the power spectra of low and high degrees are more balanced, but the Southern hemisphere reconstruction on the CMB has much less higher order structure compared to the GUFM1 model and is dominated by spherical harmonic degrees 3 and 4 (Nilsson et al., 2014).

I then chose the CALSK family for this work. The model GUFM1 was chosen to perform robustness tests.

4.3 Archeomagnetic field models - The CALS3k family

4.3.1 Methodology and data set

The Continuous Archeomagnetic and Lake Sediment (CALSxk) field models were constructed for two intervals: for the last 3000 years (models 3k) and 7000 years (models 7k). The later (Korte and Constable, 2005) were developed using archeomagnetic and lake sediments data of direction and intensity (Korte et al., 2005). Although the models describe the geomanetic field continuously with time, the Gauss coefficients are heavily smoothed at the earlier times. Furthermore, the model does not fit well the last 500 years (e.g. Genevey et al., 2009) where direct data is available (Jackson et al., 2000).

The first models for the last 3000 years, CALS3k.1 (Constable et al., 2000) and CALS3k.2 (Korte and Constable, 2003), were constructed from archeomagnetic data (intensity and direction), basaltic flows, lake sediments and also incorporated direct measurements from magnetic observatories. The period of 3000 years was chosen because of the concentration of data in this time interval. The models were expanded up to spherical harmonic degree 10. The difference between (CALS3k.1) and (CALS3k.2) is the increase in the data

set. More recently, Korte et al. (2009) constructed five new models for the last 3000 years, using a new database compilation (Korte et al., 2005; Genevey et al., 2008; Donadini et al., 2009). Models ARCH3k.1 and ARCH3k_cst.1 were constructed based only on archeomagnetic data. ARCH3k.1 uses all archeomagnetic data for the last 3000 years, and ARCH3k_cst.1 uses only archeomagnetic data that pass a quality criteria filter as described by Donadini et al. (2009). In ARCH3k_cst.1 the Northern hemisphere contributes with most of the data. So, this model describes better the evolution of the geomagnetic field in this hemisphere (Korte et al., 2009). Model SED3k.1 is based only on lake sediment data. This model is very different from ARCH3k.1 and ARCH3k_cst.1 because of the low quality and low temporal resolution of lake sediment data. Models CALS3k.3 and CALS3k_cst.1 were developed using all data available, without and with a quality criteria filter of the data set, respectively. Korte et al. (2009) concluded that the CALS3k.3 is the most adequate model for global studies. More recently, Korte and Constable (2011) used the same methodology of the five previous models to calculate models CALS3k.4 and CALS3k.4b. These new models better fit the Gauss coefficients due to an improved database. These models are expanded up to degree 10 and the temporal resolution of them is 10 years. The models are constrained by GUFM1 (Jackson et al., 2000) for the period between 1840 AD and 1990 AD.

4.3.2 Limits of CALS3k.4 and CALS3k.4b models

Spherical harmonics correspond to a set of solutions to Laplace's equation in three dimensions represented in a system of spherical coordinates. A set of well distributed data is then necessary to construct spherical harmonic field models with good spatial resolution. But this is far from what we have nowadays with the available data set. Thus, the uneven distribution of data will affect the spatial resolution of the model. Ultimately, the spatial resolution of the models is constrained by the limit placed by crustal field contamination. Therefore, the images of the magnetic field at the core surface are limited intrinsically to less than spherical harmonic degree 13, where the crustal field begins to dominate. The timescale by its turn is troubled by badly distributed data in time and principally by the errors in age estimation. Despite these limitations, the models are undoubtedly enough to describe how the magnetic field has changed over the past 3 thousands years. They are consistent with the continuous changes in space and time expected for a real magnetic

field. CALS3k.4 has spatial norm Ψ equal to 177×10^{11} nT^2 and temporal norm Φ equal to 827 nT^2yr^{-4}, while CALS3k.4b has spatial norm Ψ equal to 144×10^{11} nT^2 and temporal norm Φ equal to 583 nT^2yr^{-4} (Korte and Constable, 2011).

It is very hard to separate features that are physically real from those that arise from changes in data quality and resolution in the models. The aim here is to interpret an archeomagnetic field model and the CALS3k.4b is the best field model to investigate features at the CMB. It is the most conservative field reconstruction presently available maintaining only the most robust spatial and temporal features with lower temporal and spatial resolution. This is particularly useful for studies of field evolution at the CMB, where small-scale features including noise become enhanced compared to the Earth's surface due to the downward continuation (Korte and Constable, 2011).

4.4 Historical field model - GUFM1

4.4.1 Methodology and data set

Jackson et al. (2000) present a model of the magnetic field at the core-mantle boundary for the interval 1590-1990. The model, called GUFM1, is based on a massive compilation of historical observations of the geomagnetic field. Most of the dataset originates from unpublished observations by mariners. Care was taken to both correct the data for possible mislocation (originating from poor knowledge of longitude) and to proper estimate the error in the data (by using a stochastic model for uncorrected positional errors that properly accounts for the nature of the noise process based on a Brownian motion model). For the period before 1800, more than 83,000 individual observations of magnetic declination were recorded at more than 64,000 locations; including more than 8000 new observations for the 17th century alone. The time-dependent field model constructed from the dataset is parametrized spatially in spherical harmonics and temporally in B-splines, using a total of 36,512 parameters. The model has a good resolution of the core field, and represents the most reliable continuous model available for the historical period.

4.4.2 Limits of the GUFM1 model

The GUFM1 model is the most detailed picture of how the geomagnetic field has varied in space and time over the past 400 years, but it has also limitations, in particular those

due to the changing in quality/quantity and distribution of observations with time. The GUFM1 model becomes increasingly complex with time; the smallest features become more and more visible, especially in the last 20 years when satellite data are available. Problems pointed out for models CALS3k.4 and CALS3k.4b for spherical harmonic models are naturally also a problem to GUFM1. But GUFM1 has a way better distributed data set in time and space. GUFM1 has spatial norm Ψ equal to $35 \times 10^12\ nT^2$ and temporal norm Φ equal to $68 \times 10^3\ nT^2yr^{-4}$ (Jackson et al., 2000).

If one really wants to identify whether RFPs are robust features, the proper way is to do resolution tests involving data rather than test the models themselves. But this would demand an effort that is beyond the scope of this work. An easier alternative was taken that involves the use of filtered versions of GUFM1 to check which RFP's are missed/resolved. Although not definitive, this test provides at least a partial answer to the resolution issues of archeomagnetic field models.

Chapter 5

Results

The archeomagentic model CALS3k.4b of Korte and Constable (2011) for the interval 990 BC until 1990 AD was used to track RFPs. To test the robustness of archeomagnetic RFPs, I compared results from CALS3k.4b and GUFM1 for the period 1840 to 1990 AD. For both models a regular grid on the CMB of 1° in longitude and latitude for snapshots every 10 years was used. These correspond to much finer lengthscale than the original field models, ensuring that no information was lost as a result of the griding procedure.

5.1 Identification and tracking

Figure 5.1 illustrates the performance of the identification algorithm using three snapshots of the radial archeomagnetic field model on the CMB. The magnetic equator is marked by a solid black line, and each identified RFP is marked by an X symbol. The algorithm for mapping the magnetic equator successfully resolves the magnetic hemispheres, defines local polarity and correctly identifies RFPs that reside on the geographic equator. Therefore, RFPs are never considered partly normal, partly reversed. This is exemplified by an RFP that resides on the geographic equator below eastern Africa in Figure 5.1a.

Figure 5.1b shows an example of an especially complicated case for the mapping of the magnetic equator. For some longitudes the magnetic equator is crossed three times. In addition, the magnetic equator penetrates down to a relatively high latitude in the South. Nevertheless, the algorithm correctly maps the magnetic equator. Although the field morphology of the snapshot in Figure 5.1b is somewhat extreme, in many snapshots of the studied period a significant deviation of the magnetic equator from the geographic equator appears. The identification of magnetic hemispheres allowed the straightforward

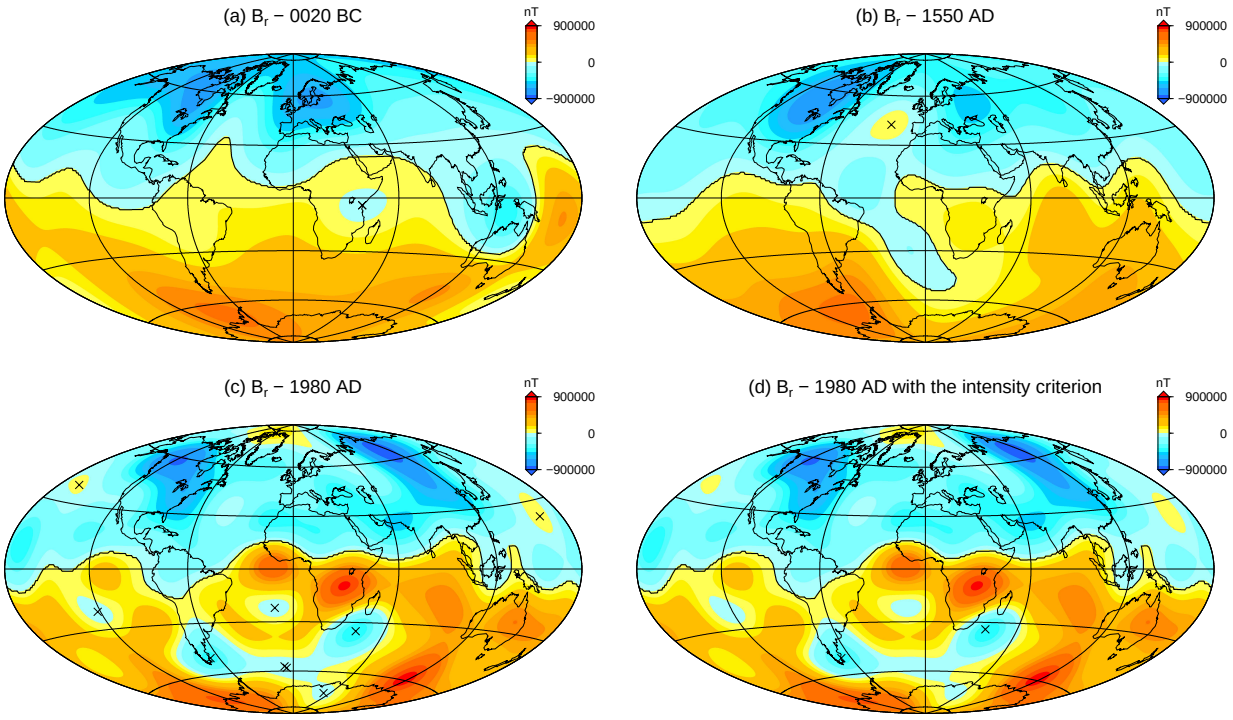

Figure 5.1: Radial geomagnetic field on the CMB at (a) 0020 BC, (b) 1550 AD and (c) 1980 AD based on the CALS3k.4b archeomagnetic field model of (Korte and Constable, 2011). The black line is the mapped magnetic equator, and the black X symbols are the peaks of the RFPs. The RFPs identification for 1980 AD with the intensity criterion is given in (d).

mapping of regions of reversed flux. Furthermore deep intrusions of normal polarity field to the opposite hemisphere as a result of undulations of the magnetic equator were correctly interpreted as normal flux. This is exemplified by a large normal polarity intrusion south of the geographic equator but north of the magnetic equator that is correctly identified as a region of normal flux in Figure 5.1b.

Some RFPs are very weak, as evidenced in Figure 5.1c. Two of these peaks (at high-latitudes of the southern Atlantic Ocean) are very close to each other. Accounting for these weak peaks might bias the tracking of RFPs. Therefore, an intensity criterion was applied in Figure 5.1d (compare with Figure 5.1c). Figures 5.1d contains two peaks of intense RFPs in the Southern Hemisphere. These two RFPs are part of a large area of reversed flux over the Atlantic Ocean, South America and Antarctica.

Figure 5.2 presents the tracking of RFPs that pass the intensity criterion. They were separated into two intervals with different RFPs activity. For all intervals, I tracked longitude and co-latitude (Fig. 5.2). The first interval is from 990 BC to 550 AD (Figs. 5.2a and 5.2c) and the second from 1450 AD to 1990 AD (Figs. 5.2b and 5.2d). No patches were

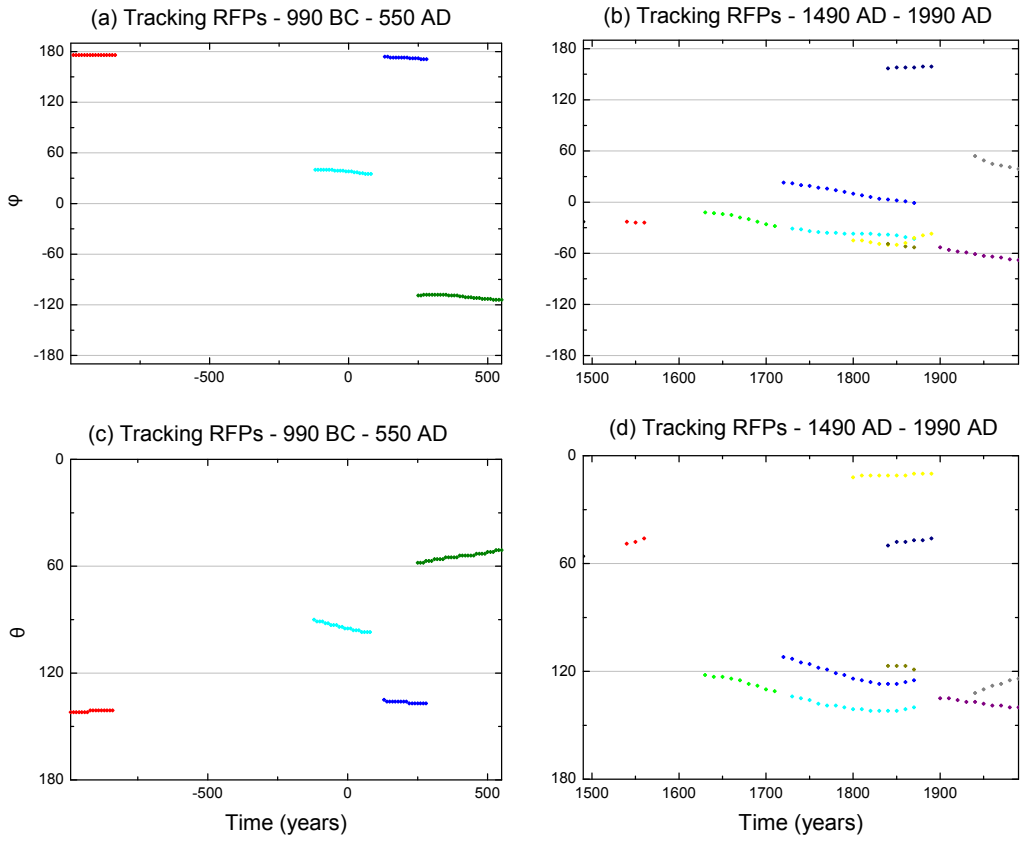

Figure 5.2: Temporal evolution of the longitude (a) and (b), and co-latitude (c) and (d) of peaks of intense RFPs in the model CALS3k.4b (Korte and Constable, 2011). (a) and (c) are from 990 BC to 550 AD; (b) and (d) are from 1490 AD to 1990 AD. The same colours are used for longitude and co-latitude of a given RFP. Longitudes and co-latitudes are given in degrees. All curves are dotted; In (a) and (c) the dotted lines seem solid due to the large period covered.

observed between these two intervals, comprising the period 550 AD - 1440 AD. From 990 BC to 550 AD, four RFPs were identified and tracked. In this period, I found two nearly stationary RFPs (red and blue) and two with westward drift (green and cyan were found). The latter two RFPs exhibit motion towards higher latitudes. From 1450 AD to 1990 AD the field model is characterized by higher spatial resolution and show a much higher occurrence of RFPs. Most RFPs exhibit a westward drift, but some quasi-stationary RFPs are also observed. In addition, most RFPs migrate towards higher latitudes.

The statistical behavior of RFPs was quantified. Table 5.1 shows the average rate of azimuthal displacement per year for three types of motions: quasi-stationary, westward and eastward drifts. The critical azimuthal angular velocity distinguishing drift from quasi-stationary behavior is the quarter of the weighted average of all RFPs, with the weighting being proportional to the lifetime of each RFP. A more forward approach would be to use

Table 5.1 - Types of RFPs azimuthal motions and the rate of their displacement per year.

	Non-filtered		f8/11		f5/11		f3/8	
	N_{RFPs}	Rate	N_{RFPs}	Rate	N_{RFPs}	Rate	N_{RFPs}	Rate
Quasi-stationary	2	-0.01	3	-0.01	4	-0.01	2	-0.02
Westward	9	-0.10	10	-0.09	8	-0.09	3	-0.17
Eastward	2	0.07	1	0.02	2	0.04	0	0

N_{RFPs} is the number of RFPs. The f8/11, f5/11 and f3/8 are filtered model in spherical harmonic degrees between 8 and 11, 5 and 11 and 3 and 8, respectively. Each rate is given in $^\circ/year$. Quarter of the average of rate is the critical value to distinguish quasi-stationary and drifting features.

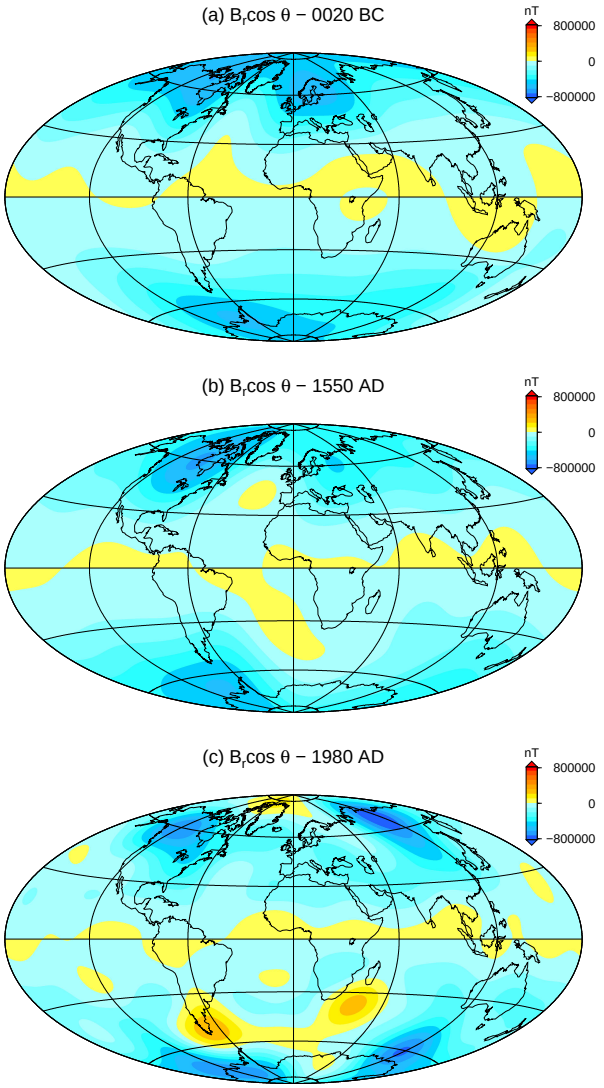

Figure 5.3: Local contributions to the ADM $B_r \cos\theta$ at (a) 0020 BC, (b) 1550 AD and (c) 1980 AD

average minus one standard deviation but this is not possible because the distribution of RFPs azimuthal angular velocity is non-Gaussian. RFPs that have angular velocity higher than this critical value are considered drifting. Table 5.1 indicates that the RFPs exhibit more a westward drift than other kind of azimuthal motions. Quasi-stationary motion occurs much less and the number of RFPs with eastward drift is the lowest. Finally, the rate of westward drift is significantly larger than the rate of eastward drift.

5.2 *Dipole changes*

Spatial contributions by normal or reversed flux to the ADM were mapped using the integrand of Equation (3.1), $B_r cos\theta$. Positive values denote opposite contributions to ADM, while negative values denote reinforcing contributions. Figure 5.3 shows local contributions to the ADM in the same years as in Figure 5.1. High-latitude intense normal flux patches provide the most important reinforcing contributions to the ADM. Mid-latitudes RFPs constitute the most significant opposite contributions to the ADM.

The mathematical definition of ADM contributions considers the geographic equator.

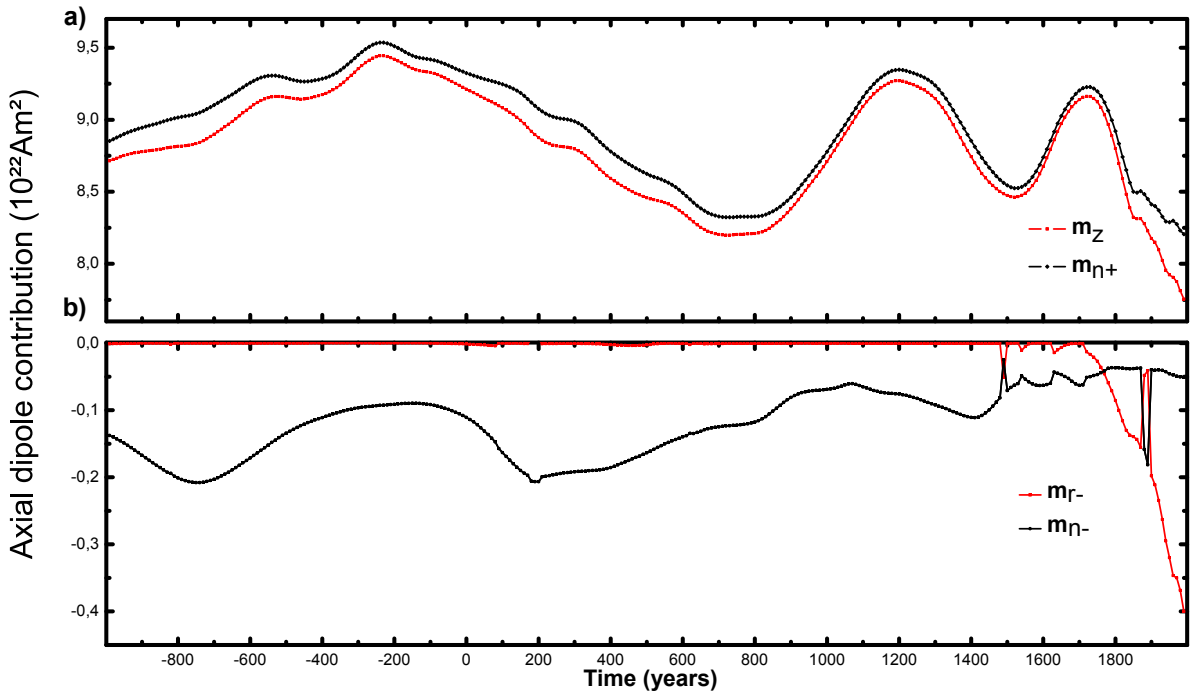

Figure 5.4: Time-dependence of ADM and its different contributions. Values of (a) total m_z and m_{n+} and (b) m_{r-} and m_{n-}. All ADM contributions are expressed in $10^{22} Am^2$. Note the difference in scales between (a) and (b).

Consequently, in Figure 5.3a below eastern Africa contributions from one RFP (Fig. 5.1a) are partly reinforcing partly opposite. Another type of opposite contribution to the ADM corresponds to areas of magnetic equator undulations. This can be seen for example in Figure 5.3b below the southern Atlantic Ocean, where normal flux associated with a deep magnetic equator intrusion (Fig. 5.1b) yields an opposing contribution to the ADM. In Figure 5.3c there are two regions of significant opposite contribution for the ADM, one below Patagonia and the other below South Africa. These structures correspond to intense RFPs on the CMB (see Fig. 5.1d).

Figure 5.4 shows the total ADM (m_z) and its contributions (3.2), including reinforcing contributions by normal flux (m_{n+}), opposite contributions by normal flux due to magnetic equator undulations (m_{n-}), and opposite contributions by reversed flux (m_{r-}). The reinforcing contributions by reversed flux (m_{r+}) were found to be negligible. The absolute values of m_z and m_{n+} (Fig. 5.4a) are much higher than those of m_{r-} and m_{n-} (Fig. 5.4b),

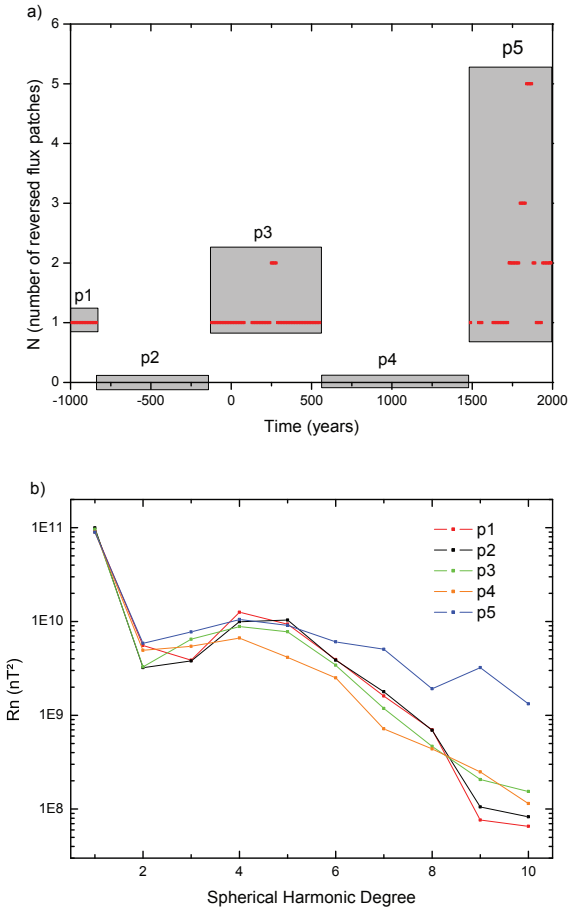

Figure 5.5: (a) Number of RFPs as a function of time. The five grey rectangles separate five periods. (b) Time-average power spectra for each period in (a).

but the temporal variations of the latter contributions are not negligible. From 990 BC until about 1800 AD the trend of ADM changes is dominantly controlled by high-latitude normal patches. The ADM changes in this period show no correlation with m_{n-} changes. However, the small diferences between m_{n+} and m_z are associated with changes in m_{n-}. In 1730 AD I detected the most recent local maximum (in absolute value) of m_z and m_{n+} with $9.14 \times 10^{22} Am^2$ and $9.23 \times 10^{22} Am^2$, respectively (Fig. 5.4a). In 1990 AD the corresponding values decreased to $7.75 \times 10^{22} Am^2$ and $8.19 \times 10^{22} Am^2$, respectively.

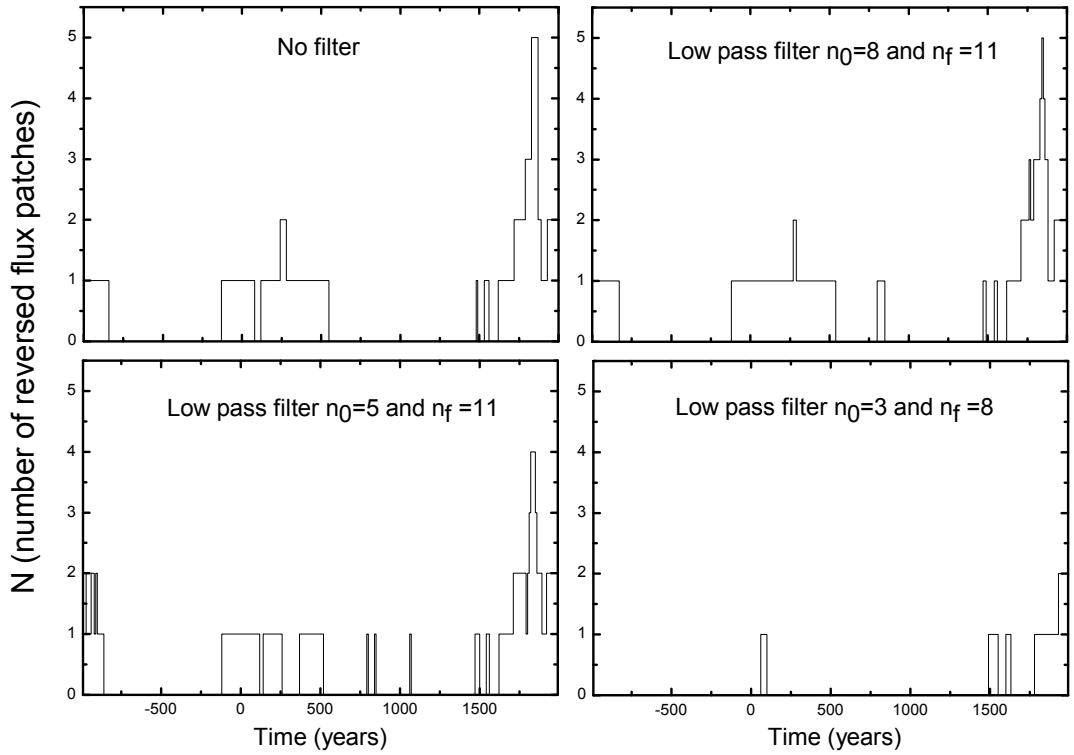

Figure 5.6: Number of RFPs as a function of time in the filtered field models.

Between 990 BC and 1760 AD RFPs have little impact on ADM changes and m_{r-} is negligible (Fig. 5.4b). The values of m_{n-} are non-negligible, but changes of trend and absolute values of m_{n-} are one order of magnitude too low to play a major role in the ADM changes (compare scales between Figs. 5.4a and 5.4b). The influence of RFPs started to overcome the influence of magnetic undulations at ∼1770 AD with an increasing trend until 1990 AD. The m_{r-} absolute value was $0.40 \times 10^{22} Am^2$ in 1990 AD, which corresponds to about 5% of the total ADM in this year. While this absolute value of m_{r-} may seem low, the difference between the total ADM change m_z and the normal flux reinforcing contributions m_{n+} increases from 1790 to 1990 AD (Fig. 5.4b) mostly due to the increase

in amplitude of the opposite contributions by m_{r-}.

5.3 Robustness tests

Figure 5.5a shows the number of identified RFPs as a function of time. Five periods of time were considered: p1 (990 BC - 840 BC), p2 (830 BC - 140 BC), p3 (130 BC - 550 AD), p4 (560 AD - 1480 AD) and p5 (1490 AD - 1990 AD). In periods p1, p3 and p5 RFPs were found, with p5 having the highest number of RFPs. In periods p2 and p4 no RFPs were found. Fig. 5.5b shows time-average power spectra of intervals identified in Fig. 5.5a. The power spectra exhibit comparable values up to spherical harmonic degree 4. The spectrum in period p4 decreases faster than the others between spherical harmonic degrees 4 and 8. Note that p4 represents almost 1000 years of absence of RFPs. The most recent period p5 has higher values for almost all spherical harmonic degrees. The earlier periods p1, p2 and p3 have a strong decrease of R_n starting in degree 6, and the periods p1 and p2 have the lowest power spectrum values for degrees 9 and 10. Note that the absence of RFPs in period p2 is not reflected in its power spectrum compared to periods p1 and p3.

The sensitivity of RFPs to uncertain small scales of the field model was studied using low pass filters with three different wavenumber bands. The filters are $n_o = 8$ and $n_f = 11$ (denoted f8/11), $n_o = 5$ and $n_f = 11$ (denoted f5/11) and $n_o = 3$ and $n_f = 8$ (denoted f3/8) (see 3.4). Figure 5.6 shows that the number of patches per year in filtered models f8/11 and f5/11 were almost the same as in the non-filtered model. Filtred model f3/8 has much lower number of patches than the others in all periods. Surprisingly, some new RFPs emerged in models f8/11 or f5/11. Moreover the total number of patches was even slightly higher in f8/11 than in the non-filtered model. More specifically note that the large interval of absence of patches (560 AD - 1480 AD) in the non-filtered model is abrupt in the filtered models f8/11 and f5/11, even though this interval is characterized by low values of R_n for spherical harmonic degrees higher than 4 (Fig. 5.5b). How does the filters could change the spatial behavior of the RFPs? To answer this question, the coordinates of RFPs were time-tracked in the filtred models and compared with the different unfiltered field models (Figs. 5.7 and 5.8). Figures 5.2a, 5.2b and 5.7a show similar results between filtered model f8/11 and the non-filtered one, with dominance of westward drift. In addition, some new

RFPs are occasionally identified and others showed a longer lifetime than in the non-filtered model. Figure 5.7b shows that filtered model f5/11 is also characterized by westward drift and a quasi-stationary behaviour with most RFPs exhibiting a somewhat shorter lifetime. Figures 5.7c and 5.8c show the action of the strongest filter. Only five RFPs were tracked in this case, three of them with westward drift and two were quasi-stationary (Table 1). The time-dependence of co-latitude of RFPs (Figures 5.2c, 5.2d and 5.8) is rather similar in non-filtered, f8/11 and f5/11 models, where most RFPs migrate towards higher latitudes. The most prominent examples include a low-latitude RFP migrating southward between 120 BC and 80 AD, a high-latitude RFP moving northward between 210 AD and 550 AD, and several mid-latitudes RFPs heading southward from 1630 AD to the present.

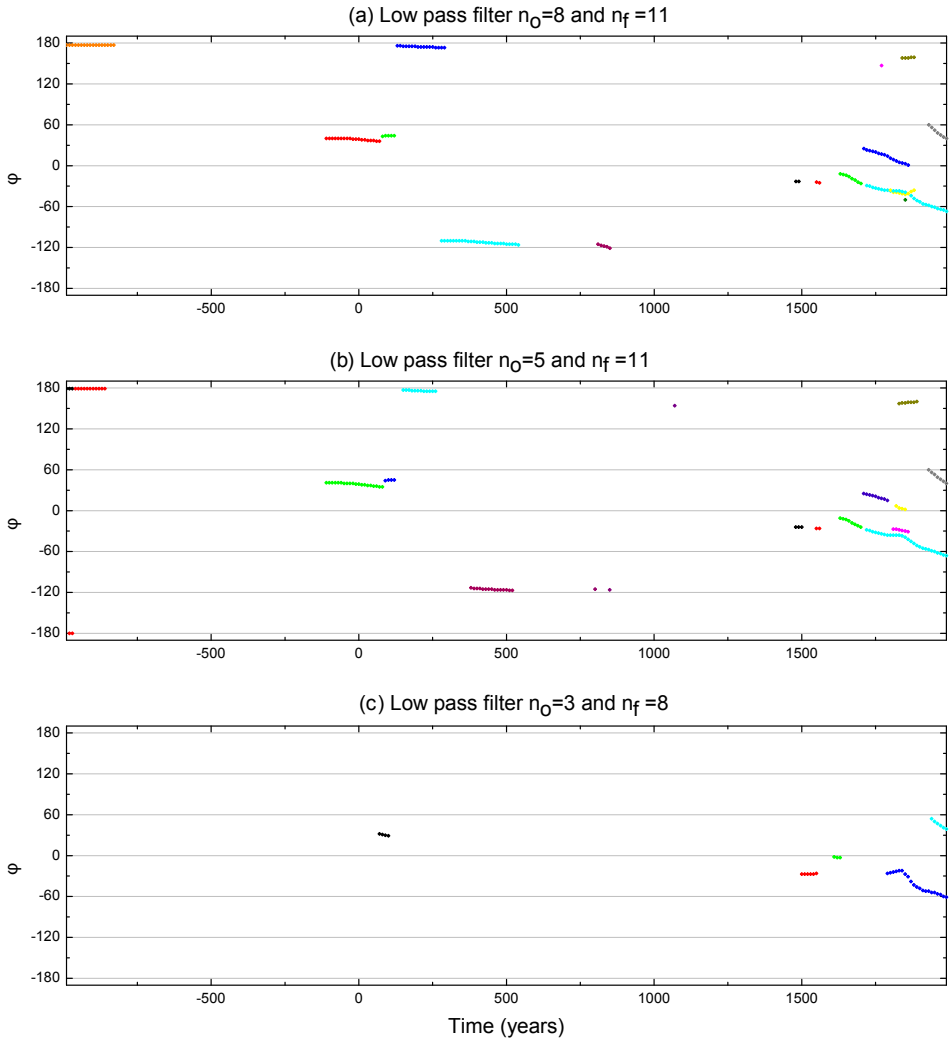

Figure 5.7: As in Fig. 5.2a and 5.2b for the filtered field models.

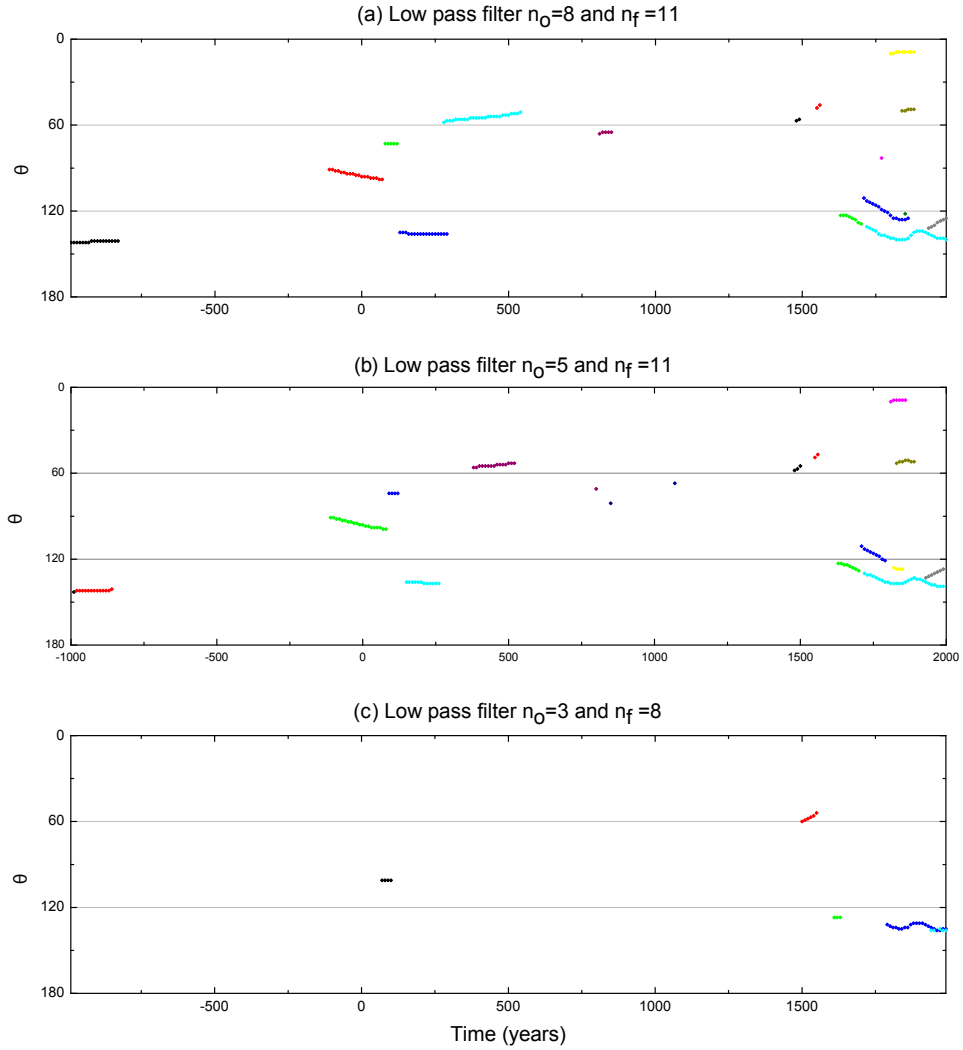

Figure 5.8: As in Fig. 5.2c and 5.2d for the filtered field models.

5.4 *Comparison with the historical field*

To test the robustness of archeomagnetic RFPs, results from CALS3k.4b and GUFM1 were compared for the period 1840 to 1990 AD (Figs. 5.9 and 5.10). Overall there is a very good agreement between RFPs tracking in both field models. Stronger filters yield even more coincident RFPs positions and motions between the two models. As with CALS3k.4b, most RFPs in GUFM1 and their filtered versions exhibit westward drift and migrate towards higher latitudes, while some RFPs are characterized by a quasi-stationary behavior.

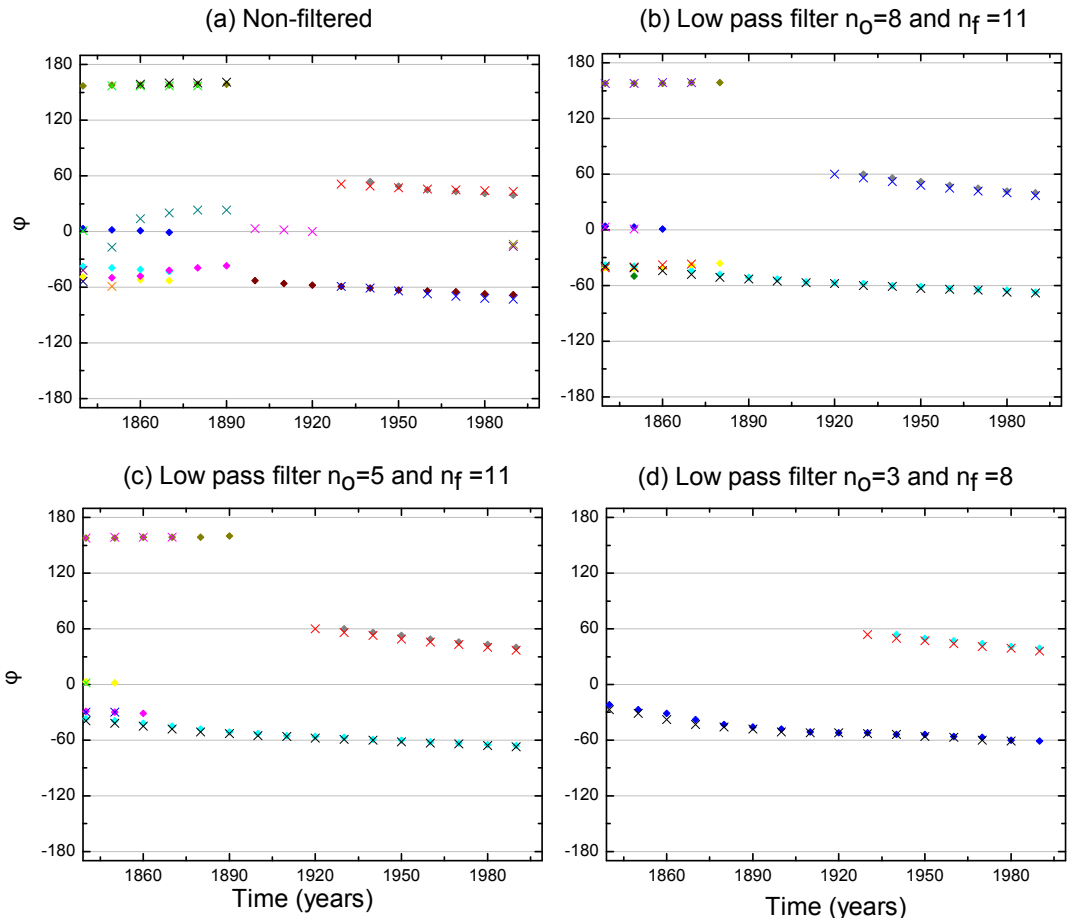

Figure 5.9: As in Fig. 5.2a and 5.2b for the period 1840-1990 AD for the filtered field models of GUFM1 and CALS3k.4b. X/diamonds represent RFPs of GUFM1/CALS3k.4b respectively.

5.5 *An unusual event of magnetic equator intrusion: formation and cut*

The archeomagnetic field model exhibits a rather unusual sequence of morphologies towards the end of the 19th century below Brazil, which may deserve a separate topic. It shows an intrusion of the magnetic equator into the Southern hemisphere followed by the formation of a RFP. Figure 5.11 shows four snapshots of B_r from 1870 AD to 1900 AD. The streamfunction of the purely helical core flow model of Amit and Olson (2004) is superimposed. In 1870 AD below Brazil a mild magnetic equator undulation of negative normal flux is very close to a large region of reversed flux which contains three RFPs, leaving a thin belt of positive normal flux in this region (Fig. 5.11a). This belt is associated with westward flow. In 1880 AD (Fig. 5.11b) the magnetic equator undulation merges within the reversed flux region, forming a large and deep magnetic equator intrusion into the southern hemisphere. The negative flux region below Brazil is now defined as normal

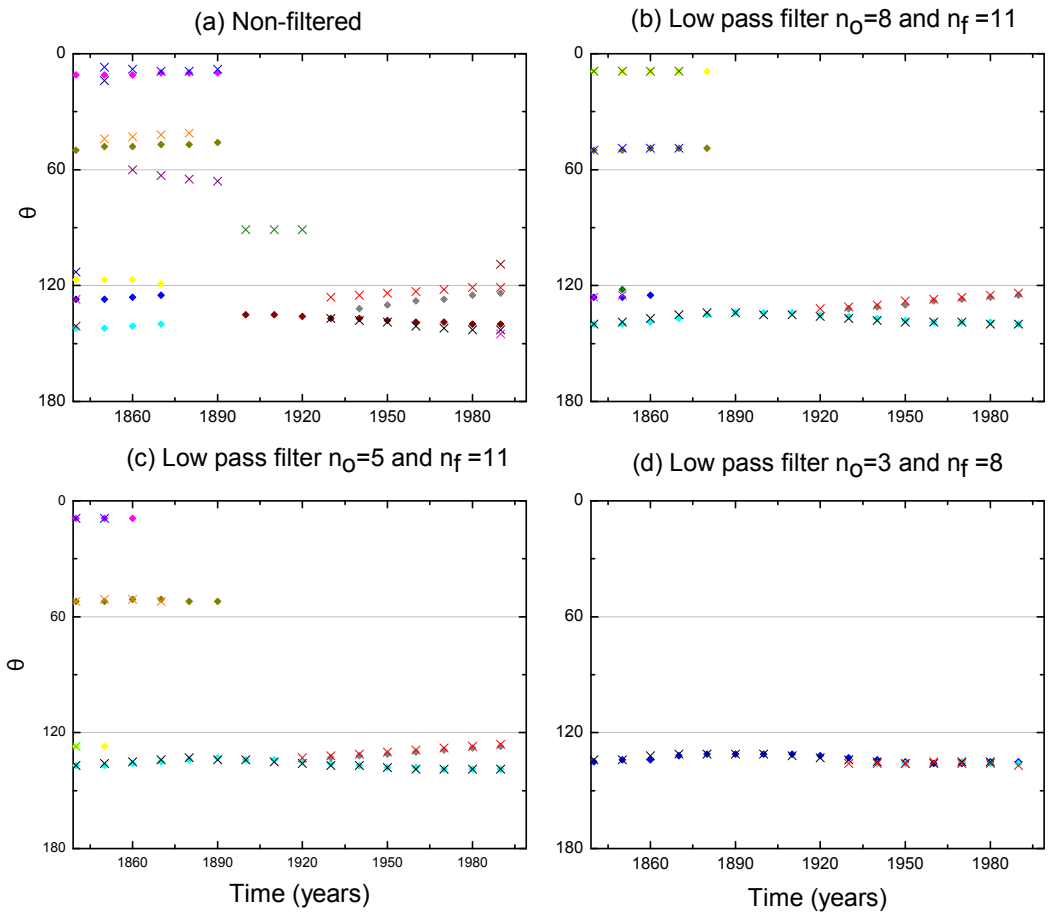

Figure 5.10: As in Fig. 5.2c and 5.2d for the period 1840-1990 AD for the filtered field models of GUFM1 and CALS3k.4b. X/diamonds represent RFPs of GUFM1/CALS3k.4b respectively.

polarity as a consequence of the peculiar topology of the magnetic equator. The core flow pattern is still westward, perpendicular to the thin neck connecting the negative flux region below Brazil to the northern hemisphere. In 1890 (Fig. 5.11c) the magnetic equator intrusion persists, but the core flow slightly turns to the north-west near the neck. In 1900 AD (Fig. 5.11d) the core flow model is perpendicular to the normal polarity belt. The magnetic equator intrusion is cut, leaving an RFP below Patagonia.

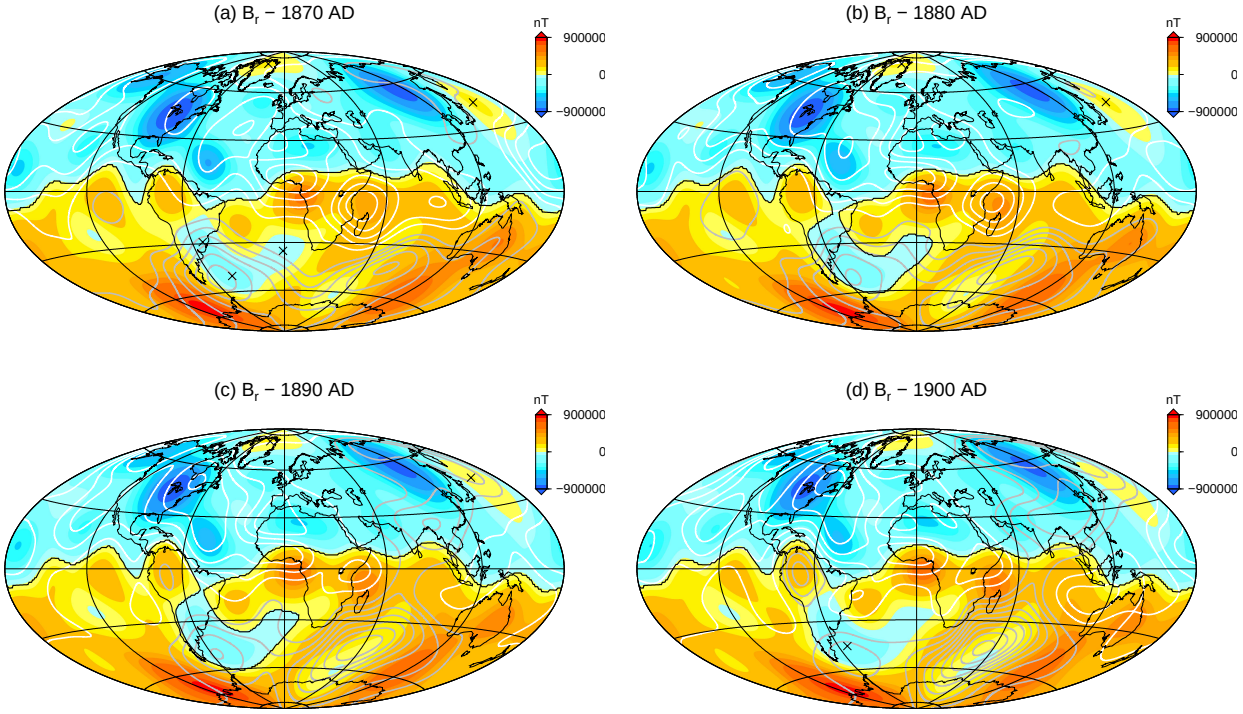

Figure 5.11: The radial geomagnetic field on the CMB at 1870 AD (a), 1880 AD (b), 1890 AD (c) and 1990 AD (d). The contours of the streamfunction of the purely helical core flow model of Amit and Olson (2004) are superimposed in all snapshots. Grey contour lines represent anti-clockwise circulation and white contour lines represent clockwise circulation. The black line is the mapped magnetic equator line, and the X symbols are the peaks of intense RFPs.

Chapter 6

Discussion and conclusions

The new definition of the local polarity based on the magnetic equator proposed here resulted in an accurate identification of reversed flux patches (RFPs). The intensity criterion filtered out weak RFPs and the velocity criterion connected adequately RFPs in successive snapshots, thus providing meaningful tracking results. Defined this way, RFPs could even be identified on the geographic equator.

One of the earliest and most prominent observations of geomagnetism was the westward drift of field structures (e.g. Bullard et al., 1950; Yukutake, 1967; Bloxham and Gubbins, 1985b; Finlay and Jackson, 2003). Although the core flow is probably more complex, the zonal part of core flow models is often westward at low- and mid-latitudes, in particular in the southern hemisphere (Amit and Olson, 2006). The dynamical origin of this westward drift is still debated. Recently, it was argued that the westward drift is caused by the gravitational coupling between the inner-core and the mantle (Aubert, 2013; Aubert et al., 2013). I found that most RFPs exhibit westward drift, but some are quasi-stationary. In Table 5.1, I quantified the azimuthal displacement rate of RFPs. The westward drifting RFPs move in an average rate of -0.10 degrees/year, a velocity that is comparable to inferred zonal core flow motions (Hulot et al., 2002; Holme and Olsen, 2006). Tracking in filtred models also showed a dominance of westward drifting RFPs, but with more quasi-stationary RFPs occurring, even though these RFPs have shorter lifetime. The azimuthal displacement rate of the RFPs changes mildly among the different filtered models, suggesting that the displacement of RFPs is not associated to the highest spherical harmonic degrees. In addition, most RFPs at both hemispheres migrated towards higher latitudes. Magnetic equator undulations in early times explain the difference between total ADM and contributions of the intense high-latitude normal flux patches. At recent times, this

difference is well explained by opposite contributions of RFPs. The reinforcing contributions of RFPs (which hypothetically may exist) were found negligible. Temporal changes in the intensity and latitude of high-latitude normal flux patches rule exclusively the trend of ADM when the field is poorly represented in terms of reversed flux regions (likely associated to low resolution of the field model). Finally, RFPs expansion and intensification since 1870 AD probably the kinematic signature of radial diffusion at the top of the outer core (Gubbins, 1987; Olson and Amit, 2006) which may indicate the presence of a thin magnetic boundary layer below the CMB (Amit and Christensen, 2008; Chulliat and Olsen, 2010).

Changes in the dipole field due to RFPs were only important after 1770 AD, which is near when CALS3k.4b is constrained by GUFM1. It is likely that RFPs should contribute continually to the dipole field but low data quality does not allow to resolve them in earlier times. The similar behavior of RFPs in CALS3k.4b and GUFM1 suggests that the spatio-temporal smoothness of the archeomagnetic field model does not prevent identification and tracking of RFPs, but its low resolution reduces the intensity of the RFPs and hence their contribution to the dipole.

Absence of RFPs in the period 550 AD - 1440 AD is related to the low geomagnetic power spectrum in spherical harmonics $n = 4 - 8$, which is associated with fewer data, resulting in a stronger effect of regularization. However, between 830 BC - 140 BC the absence of RFPs does not seem to be associated with low geomagnetic power spectrum, because the neighboring periods p1 and p3 (which have similar power spectra as period p2) contain RFPs. The absence of RFPs in the 830 BC - 140 BC period could therefore genuinely reflect a different field morphology and possibly different core dynamics in this time interval. The geomagnetic power spectrum for the recent period (p5) is much stronger than that of earlier periods because of the much better coverage and quality of the recent data.

Periods with lower values of geomagnetic power spectrum at high spherical harmonic degree lead to a larger scale field that masks small scale field morphologies. Morphologically, it implies that two neighboring regions of opposite flux would be smoothed to one region of the more intense flux. This effect creates undulations in the magnetic equator and obscures RFPs, which obscures the RFPs to ADM relationships. Perhaps surprisingly, the filtered models f8/11 and f5/11 show comparable number and more continous RFPs than the non-filtred model. This may be associated to the resolution effects. Another

possibility is that two neighboring RFPs, with low intensity values that do not pass the intensity criterion, may merge to one strong RFP after filtering and thus pass the intensity criterion. Note that the large interval of absence of RFPs (560 AD - 1480 AD) in the non-filtered model is abrupt in the filtered models f8/11 and f5/11. In these models spherical harmonic degrees 4 and 5 are not filtered whereas higher spherical harmonic degrees 9 and 10 are strongly reduced. Moreover, period p1 has the lowest values of spherical harmonic degrees 9 and 10. These results indicate that spherical harmonic degrees $n = 4-8$ strongly affect RFPs in the archeomagnetic field model. Indeed, the f3/8 filtered model strongly affects intermediate spherical harmonic degrees $n = 4 - 8$ and contains very few RFPs. Furthermore, period p4 had the lowest values of spherical harmonic degrees $n = 4 - 8$ compared to the other periods and in this period RFPs are absent (see Fig. 5.5b).

Robust tracking results common to the non-filtered as well as filtered models may shed light on the kinematics of RFPs. RFPs in all field models exhibit either a westward drift or to a much lesser extent quasi-stationary behavior. In most cases the RFPs drift to higher latitudes, thus systematically weakening the prevailing dipole polarity.

I noted an unusual event of rapid formation and cut of a magnetic equator intrusion. If the origin of this event is advective, it is expected that its formation would be associated with a local core flow perpendicular to the thin swathe separating normal flux belts, and the cut is expected to be associated with flow parallel to the intrusive normal flux neck. But the inspection of a core flow model superimposed on the magnetic maps does not reveal such patterns, suggesting that local magnetic diffusion effects at the top of the outer core (Bloxham, 1986; Bloxham and Gubbins, 1987; Amit and Christensen, 2008; Chulliat and Olsen, 2010) may possibly be responsible for the formation and cut of magnetic equator intrusions. Extra caution should be taken in such an interpretation since core flow models suffer from many uncertainties, in particular on regional scales (e.g. Holme, 2007). A third and more probable reason for the origin of this event is simply that it is an artifact from limitation in field resolution. This can be scrutinized through the observation of snapshots of model GUFM1 for the same epoch. In GUFM1 the narrow normal flux section is never closed during this time interval, showing indeed that these subtle changes are more connected to model resolution than to the core dynamics. Moreover, filtered models from CALS3k.4b also do not show this event. This event is a clear example of how resolution problems in archomagnetic field models impose some restrictions to the analysis of the

geomagentic field and how much the magnetic equator is sensible to them. Indeed, it is a tempting idea that such an event will require at least some diffusion, as there is apparently a process of merging of null-flux curves following it, but it is worth noting that this also coincides with the period where data quality increases substantially. It is more likely that the change in field structure coincides with the increase in data quality. So, the problem is that the topological algorithms would badly identify and track most RFPs for this time frame on non-filtered models. Such a case must then be explored with robustness tests.

The main conclusions of this work can be summarized as follows:

- Most RFPs exhibit westward drift.
- More than 75% of RFPs migrate towards higher latitudes.
- In some periods (but not always) the absence of RFPs is due to the low resolution of the field model. Overall, the data are not sufficient to show that RFPs were not always present in the recent few millennia.
- Filtered models and comparison with GUFM1 suggest that RFPs are prominent features of the Earth's field at the CMB.
- Spherical harmonic degrees 4 and above strongly affect the existence of RFPs.

Lastly, it is important to stress the need for new archeomagnetic data to allow for better constrained field models. Improved new models will allow to better identify and track field structures (e.g. RFPs), and consequently to advance in the understanding of RFPs and their role in core dynamics on millennial timescales.

Bibliography

Amit H., Aubert J., Hulot G., Stationary, oscillating or drifting mantle-driven geomagnetic flux patches?, J. Geophys. Res., 2010, vol. B07108, p. doi:10.1029/2009JB006542

Amit H., Christensen U., Accounting for magnetic diffusion in core flow inversions from geomagnetic secular variation, Geophys. J. Int., 2008, vol. 175, p. 913

Amit H., Korte M., Aubert J., Constable C., Hulot G., The time-dependence of intense archeomagnetic flux patches, J. Geophys. Res., 2011, vol. 116, B12106, p. doi:10.1029/2011JB008538

Amit H., Olson P., Helical core flow from geomagnetic secular variation, Phys. Earth Planet. Inter., 2004, vol. 147, p. 1

Amit H., Olson P., Time-average and time-dependent parts of core flow, Phys. Earth Planet. Inter., 2006, vol. 155, p. 120

Amit H., Olson P., Geomagnetic dipole tilt changes induced by core flow, Phys. Earth Planet. Inter., 2008, vol. 166, p. 226

Amit H., Olson P., Christensen U., Tests of core flow imaging methods with numerical dynamos, Geophys. J. Int., 2007, vol. 168, p. 27

Aubert J., Flow throughout the Earth's core inverted from gomagnetic observations and numerical dynamo models, Geophys. J. Int., 2013, vol. 192, p. 537

Aubert J., Amit H., Hulot G., Olson P., Thermo-chemical wind flows couple Earth's inner core growth to mantle heterogeneity, Nature, 2008, vol. 454, p. 758

Aubert J., Finlay C., Fournier F., Bottom-up control of geomagnetic secular variation by the Earth's inner core, Nature, 2013, vol. 502, p. 219

Aurnou J., Andreadis S., Zhu L., Olson P., Experiments on convection in Earth's core tangent cylinder, Earth Planet. Sci. Lett., 2003, vol. 212, p. 119

Backus G., Kinematics of geomagentic secular variation in a perfectly conducting core., Philos Trans R Soc Lond, 1968, vol. A263, p. 239

Backus G. E., Bayesian inference in geomagnetism, Geophys. J. R. astr. Soc., 1988, vol. 92, p. 125

Barraclough D., Gubbins D., Kerridge D., On the use of the horizontal components of the magnetic field in determining core motions, Geophys. J. Int., 1989, vol. 98, p. 293

Bloxham J., The expulsion of magnetic flux from the Earth's core, Geophys. J. R. astr. Soc., 1986, vol. 87, p. 669

Bloxham J., Gubbins D., Geomagnetic field analysis III - Magnetic fields on the core-mantle boundary, Geophys. J. R. Astr. Soc., 1985a, vol. 80, p. 695

Bloxham J., Gubbins D., The secular variation of the Earth's magnetic field, Nature, 1985b, vol. 325, p. 511

Bloxham J., Gubbins D., Thermal core-mantle interactions, Nature, 1987, vol. 325, p. 511

Bloxham J., Jackson A., Time-dependent mapping of the magnetic field at the core-mantle boundary, J. Geophys. Res., 1992, vol. 97, p. 19537

Bullard E. C., Freedman C., Gellman H., Nixon J., The westward drift of the Earth's magnetic field, Philo. Trans. R. Soc. London, 1950, vol. Ser. A, 243, p. 67

Busse F., Thermal instabilities in rapidly rotating systems, J. Fluid Mech., 1970, vol. 44, p. 441

Chulliat A., Olsen N., Observation of magnetic diffusion in the Earth's outer core from Magsat, Orsted and CHAMP data, J. Geophys. Res., 2010, vol. 115, p. doi:10.1029/2009JB006994

Constable C., Johnson C., Lund S., Global geomagnetic field models for the past 3000 years: Transient or permanent flux lobes?, Philos. Trans. R. Soc. A, 2000, vol. 358, p. 991

Courtillot V., Mouel J. L. L., Geomagnetic secular variation impulses, Nature, 1984, vol. 311, p. 709

Donadini F., Korte M., Constable C., Geomagnetic field for 0-3ka: 1. new data sets for global modeling, Geochem. Geophys. Geosys., 2009, vol. 10, p. doi:10.1029/2008GC002295.

Dormy E., Valet J., Courtillot V., Numerical models of the geodynamo and observational constrains, Geochem Geophys Geosyst 1, 2000, vol. 10, p. DOI 10.1029/2000GC000062

Dumberry M., Finlay C., Eastward and westward drift of the Earth's magnetic field for the last three millennia, Earth Planet. Sci. Lett, 2007, vol. 254, p. 146

Finlay C., Historical variation of the geomagnetic axial dipole, Phys. Earth Planet. Inter., 2008, vol. 170, p. 1

Finlay C., Jackson A., Equatorially dominated magnetic field change at the surface of Earth's core, Science, 2003, vol. 300, p. 2084

Genevey A., Gallet Y., Constable C., Korte M., Hulot G., ArcheoInt: An up graded compilation of geomagnetic field intensity data for the past ten millennia and its application to the recovery of the past dipole moment, Geochem. Geophys. Geosys., 2008, vol. 9, p. doi:10.1029/2007GC001881

Genevey A., Gallet Y., Rosen J., Le Goff M., Evidence for rapid geomagnetic field intensity variations in Western Europe over the past 800 years from new French archeomagnetic data, Earth Planet. Sci. Lett., 2009, vol. 284, p. 132

Gubbins D., Mechanism for geomagnetic polarity reversals, Nature, 1987, vol. 326, p. 167

Gubbins D., Bloxham J., Geomagnetic field analysis IV - Testing the frozen-flux hypothesis, Geophys. J. R. Astr. Soc., 1986, vol. 84, p. 139

Gubbins D., Jones A., Finlay C., Fall in Earth's magnetic field is erratic, Science, 2006, vol. 312, p. 900

Holme R., Large-scale Flow in the Core. In *Treatise on Geophysics* , vol. 8, Elsevier Science, 2007

Holme R., Olsen N., Core surface flow modelling from high-resolution secular variation, Geophys. J. Int., 2006, vol. 166, p. 518

Holme R., Olsen N., Bairstow F. L., Mapping Geomagnetic Secular Variation at the Core-Mantle Boundary., Geophys. J. Int., 2011, vol. 186, p. 521

Hulot G., Eymin C., Langlais B., Mandea M., Olsen N., Small-scale structure of the geodynamo inferred from Oersted and Magsat satellite data, Nature, 2002, vol. 416, p. 620

Hulot G., Finlay C., Constable C., Olsen N., Mandea M., The Magnetic Field of Planet Earth, Space Sci. Rev., 2010, vol. doi: 10.1007/s11214-010-9644-0

Jackson A., Finlay C., Geomagnetic Secular variation and Its Applications to the Core. In *Treatise on Geophysics* , vol. 5, Elsevier Science, 2007

Jackson A., Jonkers A., Walker M., Four centuries of geomagnetic secular variation from historical records, Phil. Trans. R. Soc. Lond., 2000, vol. A358, p. 957

Jonkers A., Jackson A., Murray A., Four centuries of geomagnetic data from historical records, Reviews of Geophysics, 2003, vol. 41, p. doi: 10.1029/2002RG000115

Kono M., Tanaka H., Mapping the Gauss coefficients to the pole and the models of paleo-secular variation, J. Geomagn. Geoelectr, 1995, vol. 47, p. 155

Korte M., Constable C., Continuous global geomagnetic field models for the past 3000 years, Phys. Earth Planet. Inter, 2003, vol. 140, p. 73

Korte M., Constable C., Continuous geomagnetic models for the past 7 millennia II: CALS7K, Geochem. Geophys. Geosyst., 2005, vol. 6(2), p. Q02H16

Korte M., Constable C., Improving geomagnetic field reconstructions for 0-3 ka, Phys. Earth Planet. Inter, 2011, vol. 188, p. 3

Korte M., Donadini F., Constable C., The Geomagnetic Field for 0-3ka: 2. A new series of time-Varying global models, J. Geophys. Res., 2009, vol. 10, p. Q06008, doi:10.1029/2008GC002297

Korte M., Genevey A., Constable C., Frank U., Schnepp E., Continuous geomagnetic field models for the past 7 millennia: 1. a new global data compilation., Geochem., Geophys., Geosys., 2005, vol. 6, p. doi:10.1029/2004GC000800

Korte M., Holme R., On the persistence of geomagnetic flux lobes in global field models, Phys. Earth Planet. Inter, 2010, vol. 182, p. 179

Licht A., Hulot G., Gallet Y., Thebault E., Ensembles of low degree archeomagnetic field models for the past three millennia, Phys. Earth Planet. Inter., 2013, vol. 224, p. 38

Lowes F., Spatial power spectrum of the main magnetic field, Geophys. J. R. astr. Soc., 1974, vol. 36, p. 717

Merrill R., McElhinny M., McFadden P., *The Magnetic Field of the Earth: Paleomagnetism, the Core, and the Deep Mantle*. Academic Press San Diego, California, USA, 1998

Moffatt H., *Magnetic Field Generation in Electrically Conducting Fluids*. Cambridge University Press Cambridge, U.K., 1978

Nilsson A., Holme R., Korte M., Suttie N., Hill M., Reconstructing Holocene geomagnetic field variation: new methods, models and implications, Geophys. J. Int., 2014, vol. 198, p. 229

Olsen N., Luehr H., Sabaka T. J., Michaelis I., Rauberg J., Tøffner-Clausen L., CHAOS-4 - A high-resolution geomagnetic field model derived from low-altitude CHAMP data, In AGU Fall Meeting, 2010, pp Abstract GP21A–0992

Olson P., Amit H., Changes in earth's dipole, Naturwissenschaften, 2006, vol. 93, p. 519

Olson P., Christensen U., The time averaged magnetic field in numerical dynamos with nonuniform boundary heat flow, Geophys. J. Int., 2002, vol. 151, p. 809

Olson P., Christensen U., Glatzmaier G., Numerical modeling of the geodynamo: Mechanisms of field generation and equilibration, J. Geophys. Res., 1999, vol. 104, p. 10383

Olson P., Sumita I., Aurnou J., Diffusive magnetic images of upwelling patterns in the core, J. Geophys. Res., 2002, vol. 107, p. doi:10.1029/2001jb000384

Pavón-Carrasco F., Osete M., Torta J., De Santis A., A geomagnetic field model for the Holocene based on archaeomagnetic and lava flow data, Earth Planet. Sci. Lett., 2014, vol. 388, p. 98

Pozzo M., Davies C., Gubbins D., Alfè D., Thermal and electrical conductivity of iron at Earth's core conditions, Nature, 2012, vol. 485, p. 355

Roberts P., Scott S., On analysis of the secular variation, 1, A hydromagnetic constraint: Theory, J. Geomagn. Geoelectr., 1965, vol. 17, p. 137

Roberts P. H., Theory of the Geodynamo. In *Treatise on Geophysics* , vol. 8, Elsevier Science, 2007

Wardinski I., Korte M., The Evolution of the core-surface flow over the last seven thousands years, J. Geophys. Res., 2008, vol. 133, p. doi:10.1029/2007JB005024.

Yukutake T., The westward drifft of the Earth's magnetic fied in historic times, J. Geomagn. Geoelectr., 1967, vol. 19, p. 93

Appendix

Appendix A

Related article in JGR

"The time dependence of reversed flux archeomagnetic flux patches". Terra-Nova, F., Amit, H., Hartmann, G. A. and Trindade, R. I. F. 2015. J. Geophys. Res. Solid Earth, 120, doi:110.1002/2014JB011742.

Received 5 NOV 2014
Accepted 14 JAN 2015
Accepted article online 20 JAN 2015

AGU PUBLICATIONS

JGR

Journal of Geophysical Research: Solid Earth

RESEARCH ARTICLE

10.1002/2014JB011742

Key Points:
- Most RFPs exhibit westward drift and almost all migrate to higher latitudes
- Advection and diffusion of RFPs explain the historical decrease in the ADM
- Spherical harmonic degrees 4 and above strongly affect the existence of the RFPs

Correspondence to:
F. Terra-Nova,
filipe.terranova@iag.usp.br

Citation:
Terra-Nova, F., H. Amit, G. A. Hartmann, and R. I. F. Trindade (2015), The time dependence of reversed archeomagnetic flux patches, *J. Geophys. Res. Solid Earth*, *120*, doi:10.1002/2014JB011742.

Received 5 NOV 2014
Accepted 14 JAN 2015
Accepted article online 20 JAN 2015

The time dependence of reversed archeomagnetic flux patches

Filipe Terra-Nova[1,2], Hagay Amit[2], Gelvam A. Hartmann[1,3], and Ricardo I. F. Trindade[1]

[1]Departamento de Geofísica, Instituto de Astronomia, Geofísica e Ciências Atmosféricas, Universidade de São Paulo, São Paulo, Brazil, [2]CNRS, Université de Nantes, Nantes Atlantiques Universités, UMR CNRS 6112, Laboratoire de Planétologie et de Géodynamique, Nantes, France, [3]Observatório Nacional, Rio de Janeiro, Brazil

Abstract Archeomagnetic field models may provide important insights to the geodynamo. Here we investigate the existence and mobility of reversed flux patches (RFPs) in an archeomagnetic field model. We introduce topological algorithms to define, identify, and track RFPs. In addition, we explore the relations between RFPs and dipole changes and apply robustness tests to the RFPs. In contrast to previous definitions, patches that reside on the geographic equator are adequately identified based on our RFPs definition. Most RFPs exhibit a westward drift and migrate toward higher latitudes. Undulations of the magnetic equator and RFPs oppose the axial dipole moment (ADM). Filtered models show a tracking behavior similar to the nonfiltered model, and surprisingly new RFPs occasionally emerge. The advection and diffusion of RFPs have worked in unison to yield the decrease of the ADM at recent times. The absence of RFPs in the period 550–1440 A.D. is related to a low in intermediate degrees of the geomagnetic power spectrum. We thus hypothesize that the RFPs are strongly dependent on intermediate spherical harmonic degrees 4 and above.

1. Introduction

The geomagnetic field is generated by convective motions of an electrically conducting fluid in the Earth's outer core. This field is observed directly since about 1590 A.D. by ships, observatories, and more recently at space by satellites [e.g., *Jackson et al.*, 2000; *Jonkers et al.*, 2003; *Hulot et al.*, 2010]. For periods preceding direct magnetic measurements, analysis of archeological and geological materials (indirect observations) provide vital information about the field. At first order, these two kinds of observations show that the field is dominated by an axial dipole. However, some nondipole features are also present, particularly in regions at the core-mantle boundary (CMB) where the polarity is opposite to that of the axial dipole (the so-called reversed flux patches, from hereafter RFPs). Expansion and intensification of these RFPs over at least the past century seem to contribute to the historical decrease in the intensity of the dipole moment [*Gubbins*, 1987].

Changes in the dipole are intrinsically related to the flow patterns of the fluid at the top of the outer core, especially to core flow features near RFPs [*Olson and Amit*, 2006; *Amit and Olson*, 2008]. Most of the radial field at the CMB is negative in the Northern Hemisphere and positive in the Southern Hemisphere. A normal flux patch has the same sign as its hemisphere, whereas an RFP has the opposite sign to its hemisphere. The most intense RFPs over the past decades are observed below the southern Atlantic hemisphere [e.g., *Jackson et al.*, 2000; *Olsen et al.*, 2010]. Direct measurements of the geomagnetic dipole intensity reveal a sustained rapid decrease since 1840 A.D. [*Gubbins*, 1987; *Bloxham and Jackson*, 1992; *Jackson et al.*, 2000; *Gubbins et al.*, 2006; *Olson and Amit*, 2006; *Finlay*, 2008]. Dipole secular variation (SV) contributes substantially to the observed field variation at Earth's surface, in particular, the steady decrease in dipole intensity over historical times. Therefore, understanding the dipole SV is crucial to understanding and perhaps predicting how the field evolves. However, it is worth noting that at its source, the CMB, dipole SV constitutes a very small part of the total SV: The SV spectrum is "blue," i.e., its power increases with harmonic degree (smaller scales).

The geomagnetic dipole intensity has been investigated using maps of the spatial contributions to the axial dipole [*Gubbins*, 1987; *Gubbins et al.*, 2006]. The temporal variability in the integrated contribution of reversed flux to the axial dipole balances its total change [*Olson and Amit*, 2006], emphasizing the role of RFPs in the decrease of dipole intensity over the historical era. However, the role of RFPs in dipole changes over millennial timescales has not yet been explored.

©2015. American Geophysical Union. All Rights Reserved.

Previous analyses of archeomagnetic field models were mostly carried out on the kinematics of high-latitude intense normal polarity flux patches. These patches were found to be mobile with alternating eastward-westward drifts [*Dumberry and Finlay*, 2007; *Wardinski and Korte*, 2008; *Korte and Holme*, 2010]. *Amit et al.* [2010] designed an algorithm for identification and tracking of intense flux patches in numerical dynamos. *Amit et al.* [2011] applied a similar algorithm for intense archeomagnetic flux patches. They found more westward drift in the Southern Hemisphere than in the Northern Hemisphere, which may indicate the impact of core-mantle thermal coupling on the geodynamo. None of these studies identified and tracked reversed archeomagnetic flux patches.

Based on theoretical arguments and numerical dynamo models, high-latitude intense normal polarity flux patches and RFPs are thought to reflect distinctive dynamical mechanisms. Rapid rotation effects in the outer core yield a flow barrier and surface convergence at the latitudes of the inner core tangent cylinder [*Aurnou et al.*, 2003]. In an α^2 dynamo, columns of fluid that are nearly invariant in the direction of the rotation axis [*Busse*, 1970] intersect the CMB at these tangent cylinder latitudes [*Olson et al.*, 1999]. Downwelling associated with columnar cyclones [*Olson et al.*, 2002; *Amit et al.*, 2007] concentrate magnetic flux to produce the high-latitude intense patches [*Olson and Christensen*, 2002]. The mobility of these robust field structures may be linked to the motion of the vortices [*Amit et al.*, 2010], so their longevity may therefore maintain the axial dipole dominance. In contrast, low- and middle-latitude RFPs could be related to the expulsion of toroidal magnetic field by deep upwelling and radial diffusion below the CMB [*Bloxham*, 1986]. If persistent, such local processes may eventually lead to a global polarity reversal [*Aubert et al.*, 2008]. These distinctive dynamo processes motivate examining the time dependence of RFPs, to compliment previous studies that described the mobility of high-latitude intense normal polarity flux patches [*Dumberry and Finlay*, 2007; *Wardinski and Korte*, 2008; *Amit et al.*, 2011].

In this paper we introduce topological algorithms to define, identify, and track RFPs. We use the CALS3k.4b archeomagnetic field model constructed for the past three millenia [*Korte and Constable*, 2011]. We explore the relation between RFPs temporal evolution and dipole changes. The robustness of the archeomagnetic RFPs is tested to assess the reliability of the identification and tracking results.

2. Methods

2.1. Identification and Tracking

The reversed flux patches (RFPs) identification method at each snapshot comprises four steps. First, the magnetic equator is identified. Second, each grid point is associated with a magnetic hemisphere. Third, peaks of RFPs are identified. Finally, an intensity criterion is invoked to filter out weak insignificant RFPs.

RFPs on the CMB are commonly defined as positive/negative radial field structures in the Northern/Southern Hemispheres [e.g., *Olson and Amit*, 2006]. This definition might be problematic. For example, a patch residing on the geographic equator is considered partly normal partly reversed. We therefore seek a more appropriate definition. In this paper, we use the magnetic equator to define the polarity at each grid point. We coded an algorithm to map the magnetic equator. At a given longitude on the CMB, the magnetic equator is defined as the point where the radial geomagnetic field B_r changes sign. To distinguish between sign changes associated with the magnetic equator or with an RFP, the algorithm searches first a longitude where there is just one point of change in the sign of B_r. This point is guaranteed to be the magnetic equator. From this initial location of magnetic equator, the algorithm selects the closest point on the neighbor longitude which has a change in sign of B_r.

After mapping the magnetic equator we define the magnetic hemispheres. Every grid point north/south of the magnetic equator is assigned to its respective magnetic hemisphere. A difficulty arises at some longitudes where the magnetic equator appears more than once. An algorithm marches from colatitude 0° to 180°, assigning the northernmost point to the northern magnetic hemisphere. Then, after every crossing of the magnetic equator, the next point is assigned to the opposite hemisphere.

Once each point on the CMB is associated with a magnetic hemisphere and a polarity (normal or reversed), the next step is to identify the peaks of RFPs. For this purpose we coded an algorithm to determine field maxima and minima of flux patches at the CMB. The algorithm searches the maxima and minima of the radial field by comparison with neighboring cells. A grid point is considered to be a maximum/minimum if it has higher/lower value than its eight neighboring cells. Maximum or minimum values indicate the coordinates (colatitude and longitude) of the peak of the RFPs at the CMB.

©2015. American Geophysical Union. All Rights Reserved.

For the final identification step we imposed a criterion of threshold intensity to avoid interpreting insignificantly weak extreme points. For every snapshot, only RFPs with peak values larger than half the most intense RFP of the same snapshot were considered. Obviously, only snapshots with more than one RFP were affected by this criterion.

To track RFPs in time, we coded an algorithm that calculates the distance of each RFP to all RFPs in the next snapshot. The spherical distance is calculated along a great circle. A critical distance was set based on typical large-scale core flow values from geomagnetic secular variation inversions. In the core flow model of *Amit and Olson* [2006], the maximum of time-averaged flow plus 1 standard deviation is about 70 km/yr. We used this value multiplied by the time step between snapshots of 10 years to obtain the critical distance for tracking. A pair of RFPs at two successive snapshots which has a spherical distance lower than this critical value is denoted as the same RFP. If an RFP in the new snapshot is farther from all previous snapshot's RFPs than the critical distance, it is denoted as a new RFP.

2.2. Dipole Changes

We took advantage of the above definitions to map local contributions to the axial dipole moment (ADM), and we investigated the temporal behavior of these contributions. The axial component of the magnetic dipole moment (m_z) is defined as follows [*Moffatt*, 1978; *Gubbins*, 1987; *Gubbins et al.*, 2006; *Olson and Amit*, 2006]:

$$m_z = \frac{4\pi a^3}{\mu_0} g_1^0 = \frac{3r_o}{2\mu_0} \int_S B_r \cos\theta \mathrm{d}S \tag{1}$$

where a is the radius of the Earth, $\mu_0 = 4\pi \times 10^7$ Hm^{-1} is the free space magnetic permeability, g_1^0 is the axial dipole Gauss coefficient, r_o is the radius of the core, B_r is the radial component of the magnetic field on the CMB, θ is colatitude and dS denotes a CMB surface increment. The integrand $B_r \cos\theta$ represents the spatial distribution of local contributions to the ADM. Thus, mapping $B_r \cos\theta$ allows imaging local contributions to the ADM.

We associate different types of $B_r \cos\theta$ structures to different ADM contributions as:

$$m_z = m_{n+} + m_{n-} + m_{r+} + m_{r-} \tag{2}$$

where the subscripts n and r denote contributions from regions of normal and reversed flux respectively, m_{n+} represents reinforcing contributions (mostly from high-latitude flux patches), m_{n-} corresponds to opposite contributions (totally from magnetic equator undulations), m_{r+} represents reinforcing contributions and m_{r-} denotes opposite contributions. Note that m_{r+} contributions appear when an RFP is localized at least partly between the magnetic equator and the geographic equator.

2.3. Robustness Tests

Uncertainties in archeomagnetic field models will produce erroneous results concerning the existence and mobility of RFPs. Robustness tests are clearly required. Two tests were performed, one using the power spectrum, the other using low-pass-filtered fields.

The Mauersberger-Lowes spectrum at the CMB is one of the primary outputs of the dynamo process in the core [*Dormy et al.*, 2000]. The magnetic field spectrum R_n at the CMB can be expressed as a function of spherical harmonic degree n in terms of the Gauss coefficients of the core field as [*Lowes*, 1974]:

$$R_n = (n+1)\left(\frac{a}{r_o}\right)^{2n+4} \sum_{m=0}^{n} \left(g_n^m\right)^2 + \left(h_n^m\right)^2 \tag{3}$$

where n is degree, m is order, and the sets g_n^m and h_n^m are the Gauss coefficients. We compared the spectrum at periods without RFPs with the spectrum at periods with RFPs to test whether the absence of patches is due to low field resolution manifested by a steeper descending spectrum.

In the second test, we defined a low-pass filter $F(n)$ by

$$F(n) = \begin{cases} 1 & , \text{if } n < n_0 \\ cos\left(\frac{n-n_0}{n_f-n_0} \cdot \frac{\pi}{2}\right) & , \text{if } n \geq n_0 \end{cases} \tag{4}$$

where n_0 marks the beginning of the filtering and n_f marks the truncation. At $n = n_f$ the filter $F(n_f) = 0$, so the highest degree considered is $n_f - 1$. We examined the sensitivity of the identification and tracking

©2015. American Geophysical Union. All Rights Reserved.

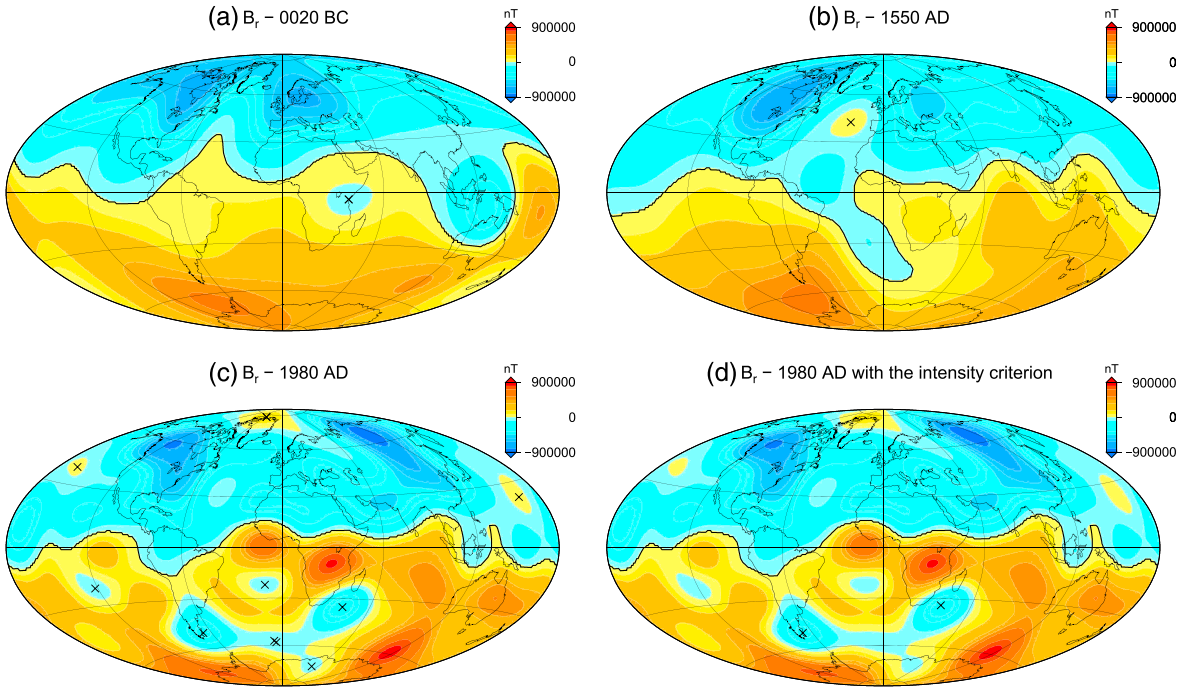

Figure 1. Radial geomagnetic field on the CMB at (a) 0020 B.C., (b) 1550 A.D., and (c) 1980 A.D. based on the CALS3k.4b archeomagnetic field model of [*Korte and Constable*, 2011]. The black line is the mapped magnetic equator, and the black X symbols are the peaks of the RFPs. (d) The RFPs identification for 1980 A.D. with the intensity criterion.

of RFPs to the small-scale field, which is most uncertain in the archeomagnetic field models, by comparing our results using the nonfiltered archeomagnetic field model with those obtained using different low-pass-filtered field models. Finally, we compare our results with the same analysis based on the historical field model GUFM1 [*Jackson et al.*, 2000] to further assess the robustness of the results from the archeomagnetic models.

3. Results

3.1. Identification and Tracking

We used the CALS3k.4b model of *Korte and Constable* [2011] for the interval 990 B.C. until 1990 A.D. This model was constructed from intensity and direction data acquired in archeological (potteries, bricks, etc.) and geological (basaltic flows and lake sediments) materials. In addition, this model is constrained by GUFM1 [*Jackson et al.*, 2000] from 1840 onward, the latter inverted from direct measurements from observatories and satellites. The database used in this model is an extension of the previous compilation of *Korte et al.* [2009]. Consequently, this model presents an improvement in the fit of the Gauss coefficients due to database updates. The model is expanded up to spherical harmonic degree 10 and the temporal resolution is 10 years. We used a regular grid on the CMB of 1° in longitude and latitude.

Figure 1 illustrates the performance of our identification algorithm using three snapshots of the radial archeomagnetic field model on the CMB. The magnetic equator is marked by a solid black line, and each identified RFP is marked by an X symbol (see Figure 1). Our algorithm for mapping the magnetic equator resolves well the magnetic hemispheres, defines local polarity, and correctly identifies RFPs that reside on the geographic equator. Therefore, RFPs are never considered partly normal partly reversed. Figure 1a shows an example of a successfully identified RFP that resides on the geographic equator below eastern Africa.

Figure 1b shows an example of an especially complicated case for the mapping of the magnetic equator. For some longitudes the magnetic equator is crossed 3 times (in other rare snapshots not shown here up to five such crossings occurred). In addition, the magnetic equator penetrates up to a relatively high latitude. Nevertheless, our algorithm correctly maps the magnetic equator. Although the field morphology of the snapshot in Figure 1b is somewhat extreme, in many snapshots of the studied period a significant deviation

©2015. American Geophysical Union. All Rights Reserved.

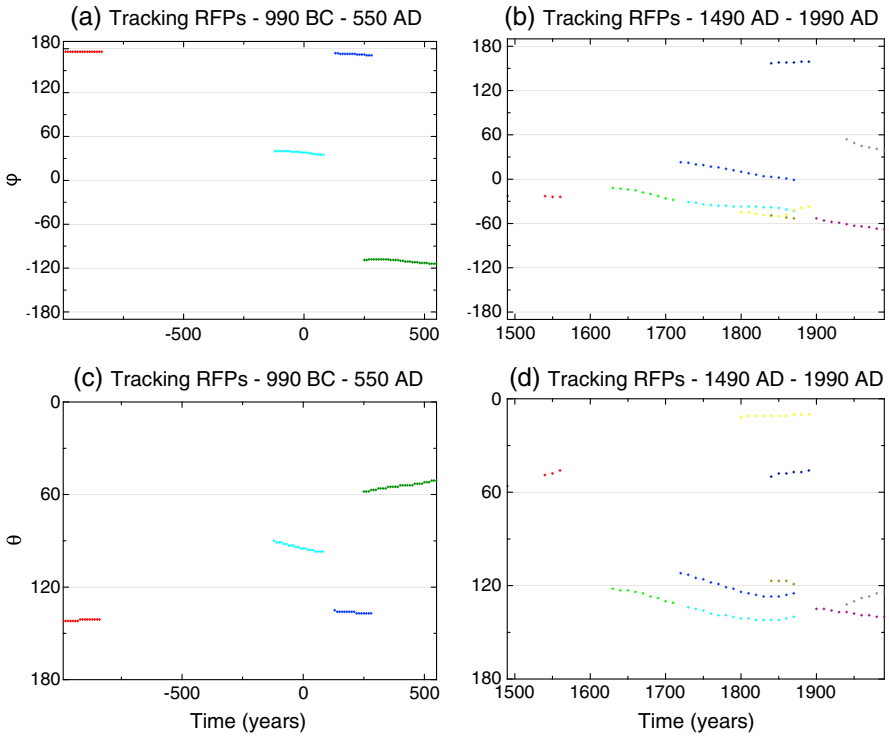

Figure 2. Temporal evolution of the (a, b) longitude, and (c, d) colatitude of peaks of intense RFPs in the model CALS3k.4b [*Korte and Constable*, 2011]. Figures 2a and 2c are from 990 B.C. to 550 A.D.; Figures 2b and 2d are from 1490 A.D. to 1990 A.D. The same colors are used for longitude and colatitude of a given RFP. Longitudes and colatitudes are given in degrees. All curves are dotted; In Figures 2a and 2c the dotted lines seem solid due to the large period covered.

of the magnetic equator from the geographic equator appears. The identification of magnetic hemispheres allowed the straightforward mapping of regions of reversed flux. Furthermore, deep intrusions of normal polarity field to the opposite hemisphere as a result of undulations of the magnetic equator were correctly interpreted as normal flux. This is exemplified by a large normal polarity intrusion south of the geographic equator but north of the magnetic equator that is correctly identified as a region of normal flux in Figure 1b.

Some RFPs are very weak, as evidenced in Figure 1c. Two of these peaks (at high latitudes of the southern Atlantic Ocean) are very close to each other. Accounting for these weak peaks might bias the tracking of RFPs. We therefore introduced in Figure 1d the intensity criterion (compare Figures 1c and 1d). Figure 1d contains two peaks of intense RFPs in the Southern Hemisphere. These two RFPs are part of a large area of reversed flux over the Atlantic Ocean, South America, and Antarctica.

The tracking of RFPs that pass the intensity criterion is separated into intervals with different RFPs activity. For all intervals, we tracked longitude and colatitude (Figure 2). The first interval is from 990 B.C. to 550 A.D. (Figures 2a and 2c) and the second from 1450 A.D. to 1990 A.D. (Figures 2b and 2d). No patches were observed between these two intervals, comprising the period 550 A.D.–1440 A.D. in Figure 2. From 990 B.C. to 550 A.D., four RFPs were identified and tracked. In this period, we found two nearly stationary RFPs (red and blue) and two with westward drift (green and cyan). The latter two RFPs exhibit motion toward higher latitudes. From 1450 A.D. to 1990 A.D. the field model is characterized by higher spatial resolution resulting in a much higher occurrence of RFPs. Most RFPs exhibit a westward drift, but some quasi-stationary RFPs are also observed. In addition, most RFPs migrate toward higher latitudes.

We quantified the statistical behavior of RFPs. Table 1 shows the average rate of azimuthal displacement per year for three types of motions: quasi-stationary, westward, and eastward. The critical azimuthal angular velocity distinguishing drift from quasi-stationary is the quarter of the weighted average of all RFPs, with the weighting being proportional to the lifetime of each RFP. We did not take the average minus 1 standard

©2015. American Geophysical Union. All Rights Reserved.

Table 1. Types of RFPs Azimuthal Motions and the Rate of Their Displacement per Year[a]

	Nonfiltered		f8/11		f5/11		f3/8	
	N_{RFPs}	Rate	N_{RFPs}	Rate	N_{RFPs}	Rate	N_{RFPs}	Rate
Quasi-stationary	2	−0.01	3	−0.01	4	−0.01	2	−0.02
Westward	9	−0.10	10	−0.09	8	−0.09	3	−0.17
Eastward	2	0.07	1	0.02	2	0.04	0	0

[a] N_{RFPs} is the number of RFPs. The f8/11, f5/11, and f3/8 are filtered models in spherical harmonic degrees between 8 and 11, 5 and 11, and 3 and 8, respectively. Each rate is given in $°/yr$. Quarter of the average of rate is the critical value to distinguish quasi-stationary and drifting features.

deviation because the distribution of RFPs azimuthal angular velocity turns out to be non-Gaussian. RFPs that have angular velocity higher than this critical value are considered drifting. Table 1 indicates that the RFPs exhibit more a westward drift than other kind of azimuthal motions. Quasi-stationary motion occurs much less and the number of RFPs with eastward drift is the lowest. Finally, the rate of westward drift is significantly larger than the rate of eastward drift.

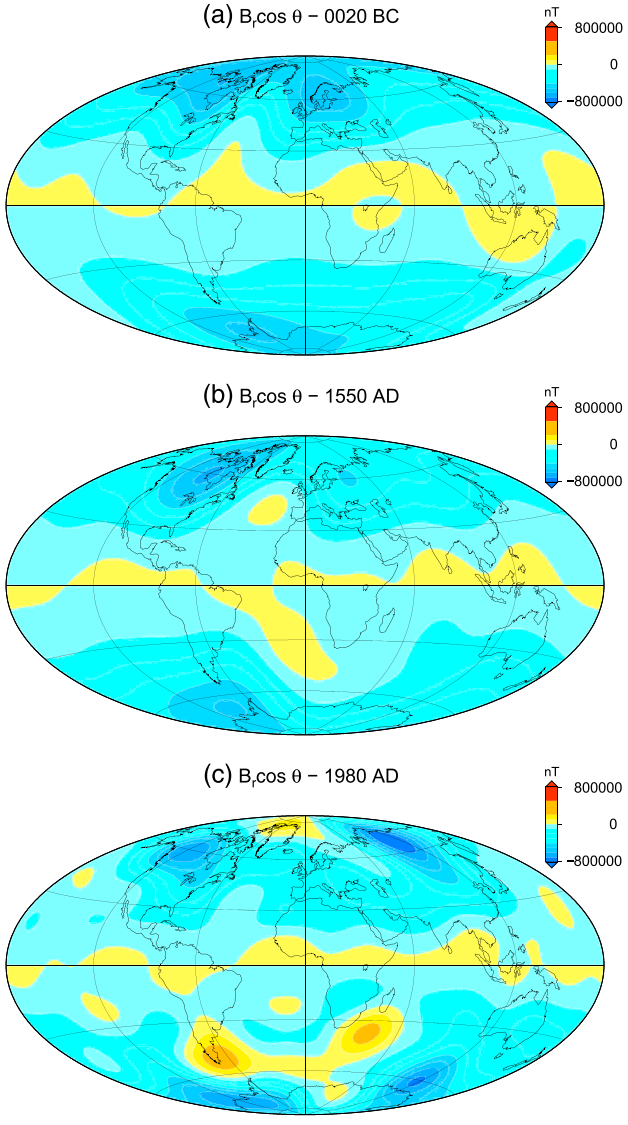

Figure 3. Local contributions to the ADM $B_r \cos\theta$ at (a) 0020 B.C., (b) 1550 A.D., and (c) 1980 A.D.

3.2. Dipole Changes

Spatial contributions (by normal or reversed flux) to the ADM were mapped using the integrand of equation (1), $B_r \cos\theta$. Positive values denote opposite contributions to ADM, while negative values denote reinforcing contributions. Figure 3 shows local contributions to the ADM in the same years as in Figure 1. High-latitude intense normal flux patches provide the most important reinforcing contributions to the ADM. Midlatitude RFPs constitute the most significant opposite contributions to the ADM.

The mathematical definition of ADM contributions considers the geographic equator. Consequently, in Figure 3a below eastern Africa contributions from one RFP (Figure 1a) are partly reinforcing partly opposite. Another type of opposite contribution to the ADM corresponds to areas of magnetic equator undulations. This can be seen for example in Figure 3b below the southern Atlantic Ocean, where normal flux associated with deep magnetic equator intrusion (Figure 1b) yields an opposing contribution to the ADM. In Figure 3c there are two regions of significant opposite contribution for the ADM, one below Patagonia and the other below South Africa. These structures correspond to intense RFPs on the CMB (see Figure 1d).

©2015. American Geophysical Union. All Rights Reserved.

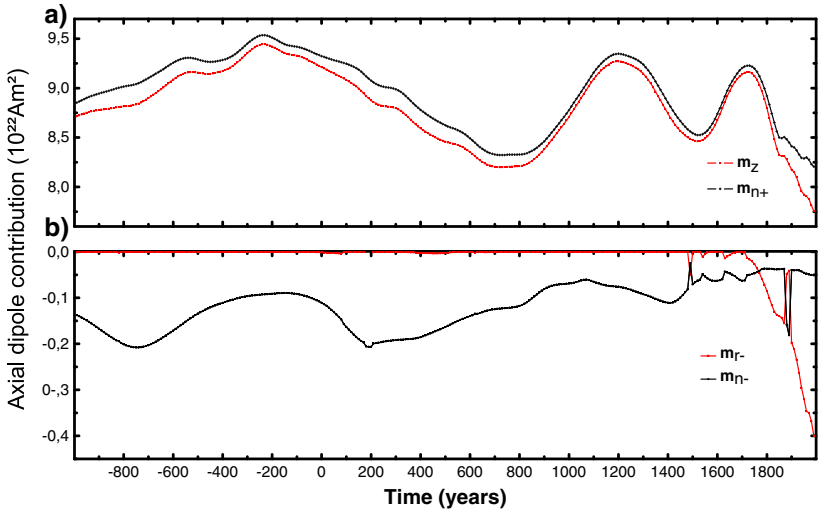

Figure 4. Time dependence of ADM and its different contributions. Values of (a) total m_z and m_{n+} and (b) m_{r-} and m_{n-}. All ADM contributions are expressed in 10^{22} A m^2. Note the difference in scales between Figures 4a and 4b.

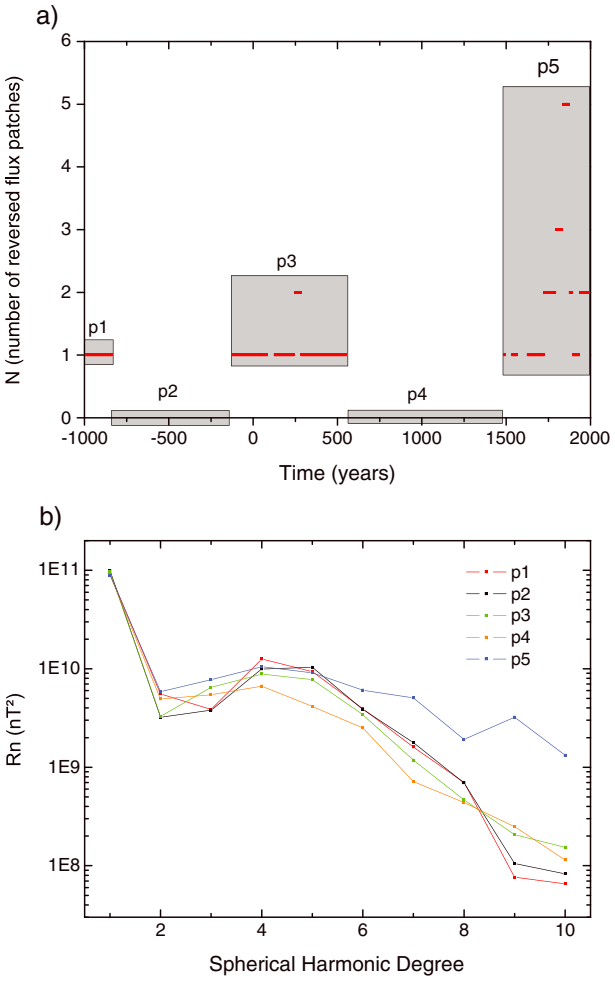

Figure 5. (a) Number of RFPs as a function of time. The five grey rectangles separate five periods. (b) Time-average power spectra for each period in (a).

Figure 4 shows the total ADM (m_z) and its contributions (2), including reinforcing contributions by normal flux (m_{n+}), opposite contributions by normal flux due to magnetic equator undulations (m_{n-}), and opposite contributions by reversed flux (m_{r-}). The reinforcing contributions by reversed flux (m_{r+}) were found to be negligible. The absolute values of m_z and m_{n+} (Figure 4a) are much higher than those of m_{r-} and m_{n-} (Figure 4b), but the temporal variations of the latter contributions are not negligible. From 990 B.C. until about 1800 A.D. the trend of ADM changes is dominantly controlled by high-latitude normal patches. The ADM changes in this period show no correlation with m_{n-} changes. However, the small differences between m_{n+} and m_z are associated with changes in m_{n-}. In 1730 A.D. we detect the most recent local maximum (in absolute value) of m_z and m_{n+} with 9.14×10^{22} A m^2 and 9.23×10^{22} A m^2, respectively (Figure 4a). In 1990 A.D. the corresponding values decreased to 7.75×10^{22} A m^2 and 8.19×10^{22} A m^2, respectively.

Between 990 B.C. and 1760 A.D. RFPs have little impact on ADM changes and m_{r-} is negligible (Figure 4b). The

©2015. American Geophysical Union. All Rights Reserved.

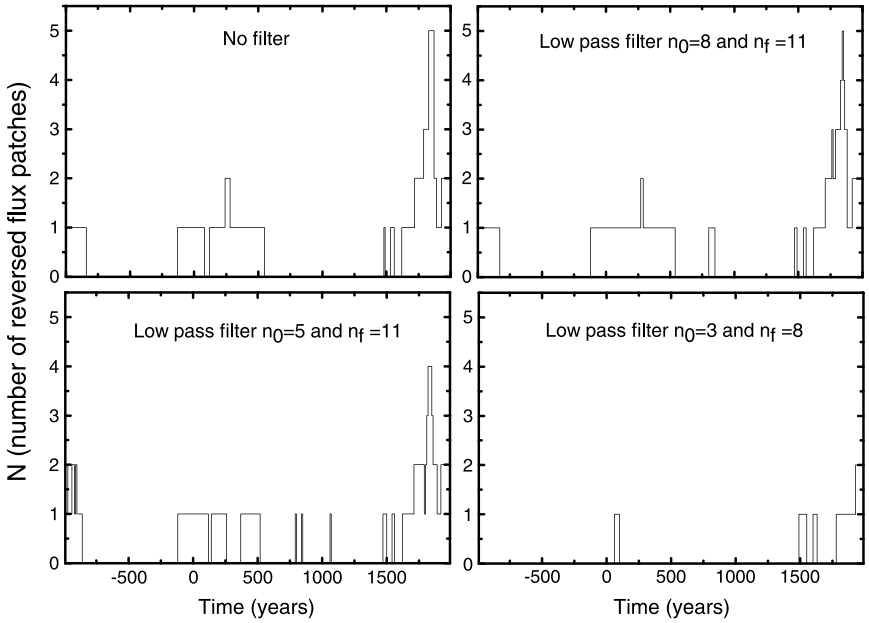

Figure 6. Number of RFPs as a function of time in the filtered field models.

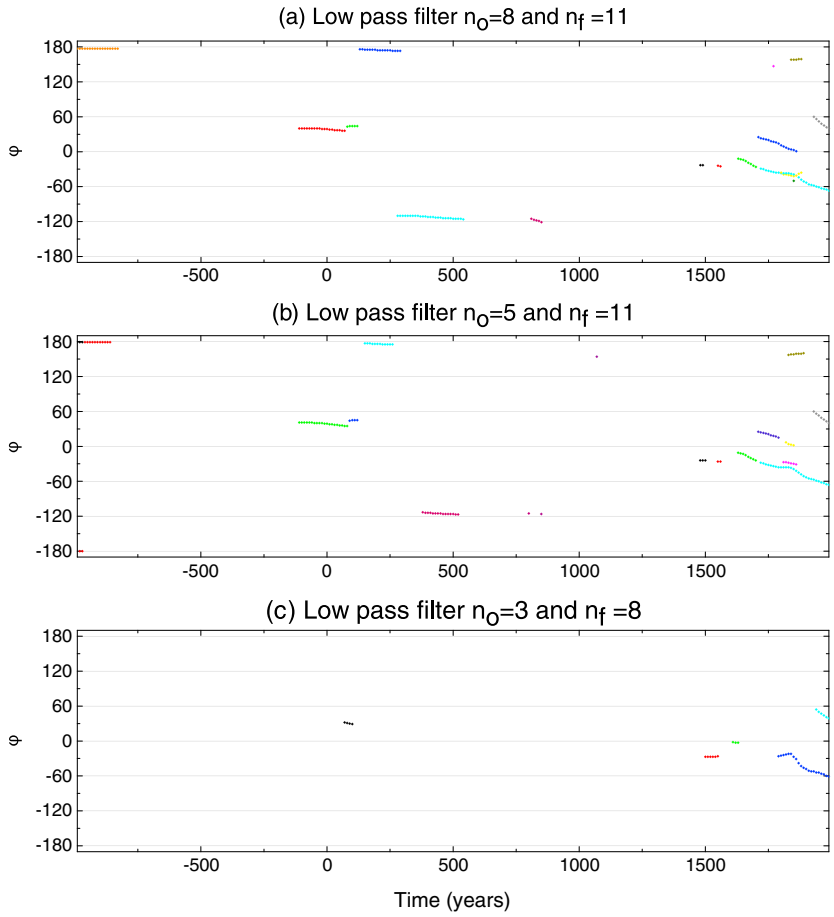

Figure 7. As in Figures 2a and 2b for the filtered field models.

©2015. American Geophysical Union. All Rights Reserved.

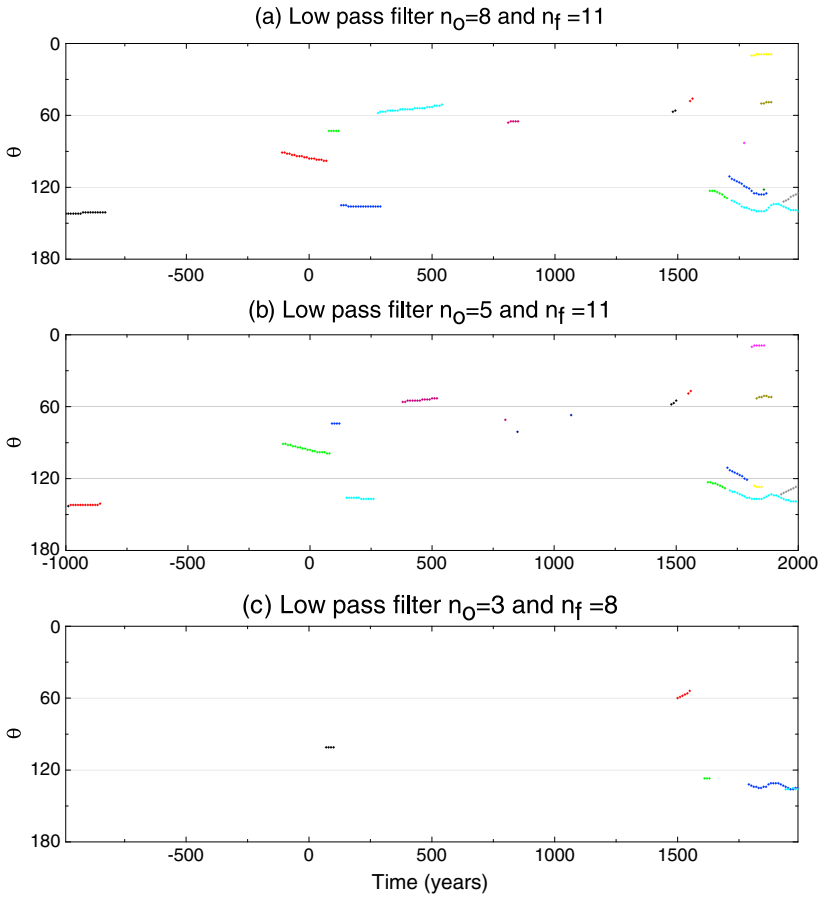

Figure 8. As in Figures 2c and 2d for the filtered field models.

values of m_{n-} are nonnegligible. However, changes of trend and absolute values of m_{n-} are an order of magnitude too low to play a major role in the ADM changes during this period (compare scales between Figures 4a and 4b). The influence of RFPs started to be higher than the influence of magnetic undulations from ~1770 A.D. with increasing trend until 1990 A.D. The m_{r-} absolute value was 0.40×10^{22} A m^2 in 1990 A.D., about 5% of the total ADM in this year. While this absolute value of m_{r-} may seem low, the difference between the total ADM change m_z and the normal flux reinforcing contributions m_{n+} increases from 1790 to 1990 A.D. (Figure 4b) mostly due to the increase in the amplitude of the opposite contributions by m_{r-}.

3.3. Robustness Tests

Figure 5a shows the number of identified RFPs as a function of time. Five periods of time were considered: p1 (990 B.C.–840 B.C.), p2 (830 B.C.–140 B.C.), p3 (130 B.C.–550 A.D.), p4 (560 A.D.–1480 A.D.), and p5 (1490 A.D.–1990 A.D.). In periods p1, p3, and p5 RFPs were found, with p5 having the highest number of RFPs. In periods p2 and p4 no RFPs were found. Figure 5b shows time-averaged power spectra of the intervals identified in Figure 5a. The power spectra exhibit comparable values up to spherical harmonic degree 4. The spectrum in period p4 decreases faster than the others between spherical harmonic degrees 4 and 8. Note that p4 represents almost 1000 years of absence of RFPs. The most recent period p5 has higher values for almost all spherical harmonic degrees. The earlier periods p1, p2, and p3 have a strong decrease of R_n starting in degree 6, and the periods p1 and p2 have the lowest power spectrum values for degrees 9 and 10. Note that the absence of RFPs in period p2 is not reflected in its power spectrum compared to periods p1 and p3.

Next we used low pass filters with three different wave number bands to study the sensitivity of RFPs to uncertain small scales of the field model. The filters are $n_o = 8$ and $n_f = 11$ (denoted f8/11), $n_o = 5$ and

©2015. American Geophysical Union. All Rights Reserved.

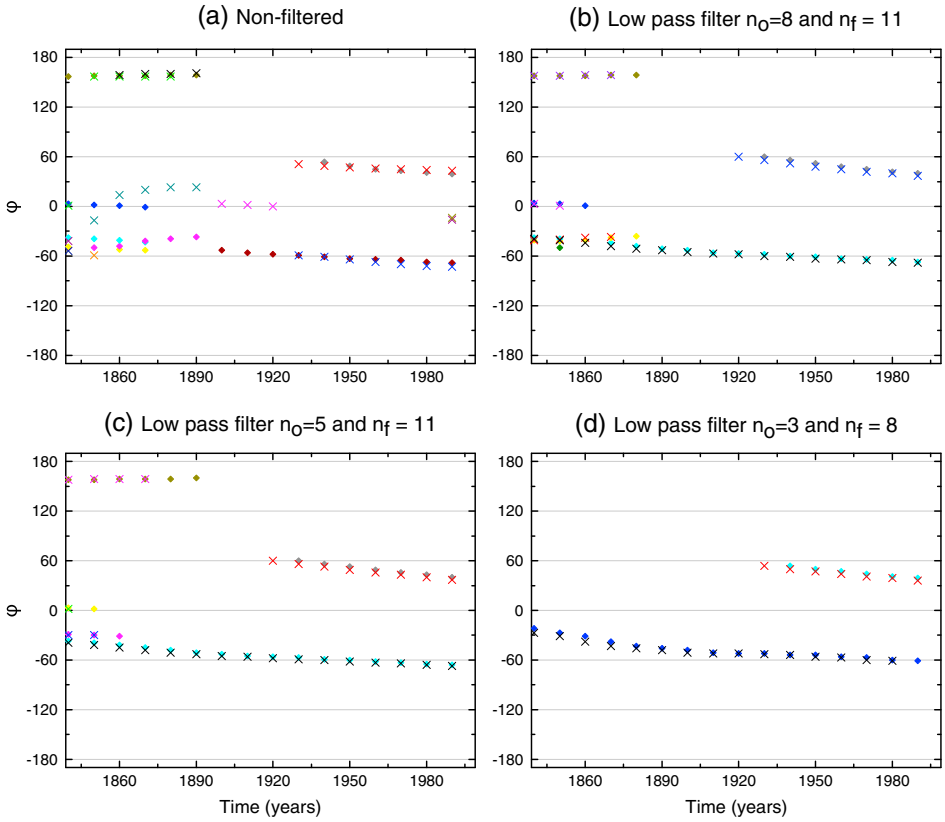

Figure 9. As in Figures 2a and 2b for the period 1840–1990 A.D. for the filtered field models of GUFM1 and CALS3k.4b. Crosses/diamonds represent RFPs of GUFM1/CALS3k.4b respectively.

$n_f = 11$ (denoted f5/11), and $n_o = 3$ and $n_f = 8$ (denoted f3/8) (see (4)). Figure 6 shows that the number of patches per year in filtered models f8/11 and f5/11 was almost the same as that in the nonfiltered model. Filtered model f3/8 has much lower number of patches than the others in all periods. Surprisingly, some new RFPs emerged in models f8/11 or f5/11. Moreover, the total number of patches was even slightly higher in f8/11 than in the nonfiltered model. More specifically note that the large interval of absence of patches (560 A.D.–1480 A.D.) in the nonfiltered model is occasionally abrupt in the filtered models f8/11 and f5/11, even though this interval is characterized by low values of R_n for spherical harmonic degrees higher than 4 (Figure 5b).

We now address the question of how the filters could change the spatial behavior of the RFPs. For this purpose, we tracked in time the coordinates of the RFPs in the filtered models and we compared the results obtained by the different field models (Figures 7 and 8). Figures 2a, 2b, and 7a show similar results between the filtered model f8/11 and the nonfiltered model, with dominance of westward drift. In addition, some new RFPs are occasionally identified and others showed a larger lifetime than in the nonfiltered model. Figure 7b shows that the f5/11 filtered model is also characterized by westward drift and quasi-stationary behavior with most RFPs exhibiting a somewhat shorter lifetime. Figures 7c and 8c show the action of the strongest filter. The low number of RFPs strongly limits the robustness of characterizing their behavior in this model. Only five RFPs were tracked, three of them with westward drift and two were quasi-stationary (Table 1). The time dependence of the colatitude of the RFPs (Figures 2c, 2d, and 8) is rather similar in the nonfiltered, f8/11 and f5/11 models: Most RFPs migrate toward higher latitudes. The most prominent examples include a low-latitude RFP migrating southward between 120 B.C.–80 A.D., a high-latitude RFP moving northward between 210 A.D. and 550 A.D., and several midlatitude RFPs heading southward between 1630 A.D. and the present.

©2015. American Geophysical Union. All Rights Reserved.

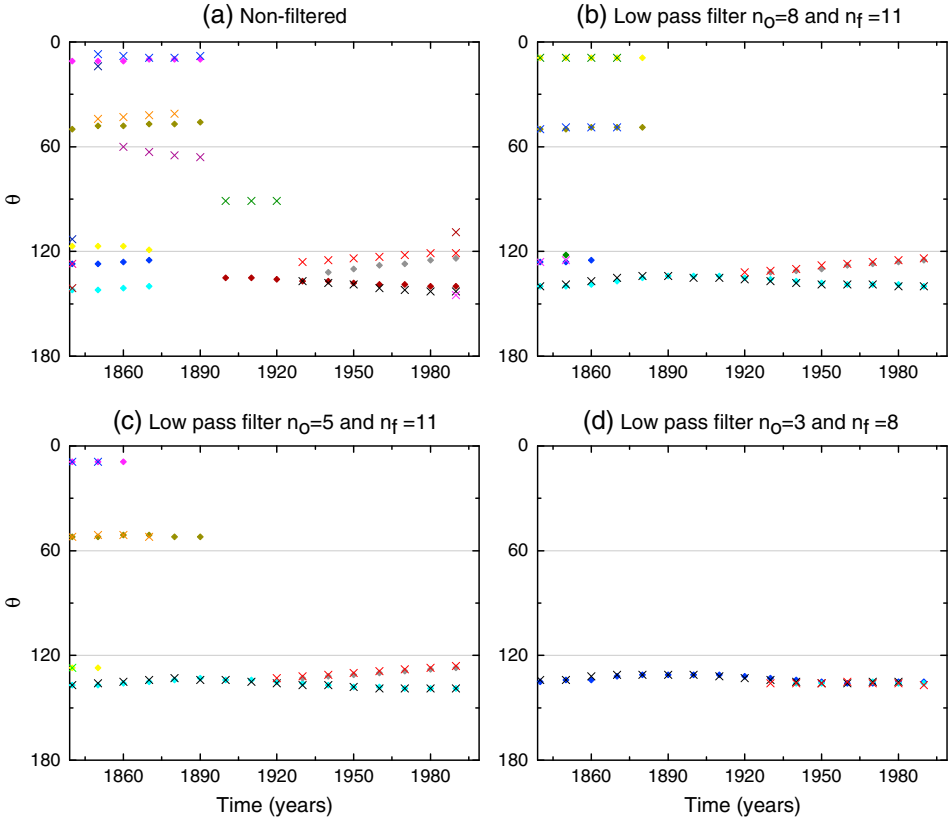

Figure 10. As in Figures 2c and 2d for the period 1840-1990 A.D. for the filtered field models of GUFM1 and CALS3k.4b. Crosses/diamonds represent RFPs of GUFM1/CALS3k.4b, respectively.

3.4. Comparison With the Historical Field

To further test the robustness of the archeomagnetic RFPs, we compare in Figures 9 and 10 results from CALS3k.4b and GUFM1 for the period 1840 to 1990 A.D. Overall, there is a very good agreement between the tracking in both field models. Stronger filters yield even more coincident RFP positions and motions between the two models. As with CALS3k.4b, most RFPs in GUFM1 and their filtered models exhibit westward drift and migrate toward higher latitudes, while some RFPs are characterized by a quasi-stationary behavior.

4. Discussion

Our definition of the local polarity based on the magnetic equator yielded accurate identification of reversed flux patches (RFPs). The intensity criterion filtered out weak RFPs and the velocity criterion connected adequate RFPs in successive snapshots, thus providing meaningful tracking results. Defined this way, RFPs could even be identified on the geographic equator.

One of the earliest and most prominent observations of geomagnetism was the westward drift of field structures [e.g., *Bullard et al.*, 1950; *Yukutake*, 1967; *Bloxham and Gubbins*, 1985; *Finlay and Jackson*, 2003]. Although the core flow is probably more complex, the zonal part of core flow models is often westward at low and middle latitudes, in particular, in the Southern Hemisphere [*Amit and Olson*, 2006]. The dynamical origin of this westward drift is still debated. Recently, it was argued that the westward drift is caused by the gravitational coupling between the inner core and the mantle [*Aubert*, 2013; *Aubert et al.*, 2013]. We find that most RFPs exhibit westward drift. In Table 1, we quantify the azimuthal displacement rate of the RFPs. The westward drifting RFPs move in an average rate of −0.10°/yr, comparable to inferred zonal core flow motions [*Hulot et al.*, 2002; *Holme and Olsen*, 2006]. Tracking in filtered models showed slightly more quasi-stationary RFPs (although still westward drifting RFPs occur more), even though these RFPs have shorter lifetime. The azimuthal displacement rate of the RFPs changes mildly among the different

©2015. American Geophysical Union. All Rights Reserved.

filtered models, suggesting that the displacement of RFPs is not associated to the highest spherical harmonic degrees. In addition, most RFPs at both hemispheres migrated toward higher latitudes.

We identified different types of possible morphological contributions to the axial dipole moment (ADM) (see Figures 3 and 4). Magnetic equator undulations in early times explain the difference between total ADM and contributions of the intense high-latitude normal flux patches. At recent times, this difference is well explained by opposite contributions of RFPs. The reinforcing contributions of RFPs (which hypothetically may exist) were found negligible. Temporal changes in the intensity and latitude of high-latitude normal flux patches rule exclusively the trend of the ADM when the field is poorly represented in terms of reversed flux regions (likely associated to low resolution of the field model). Finally, RFPs expansion and intensification since 1870 A.D. to present is probably the kinematic signature of radial diffusion at the top of the outer core [*Gubbins*, 1987; *Olson and Amit*, 2006] which may indicate the presence of a thin magnetic boundary layer below the CMB [*Amit and Christensen*, 2008; *Chulliat and Olsen*, 2010].

Changes in the dipole field due to RFPs were only important after 1770 A.D., which is near when CALS3k.4b is constrained by GUFM1. It is likely that RFPs should contribute continually to the dipole field but that low data quality does not allow to resolve them in earlier times. The similar behavior of RFPs in CALS3k.4b and GUFM1 suggests that the spatiotemporal smoothness of the archeomagnetic field model does not prevent identification and tracking of RFPs, but its low resolution reduces the intensity of the RFPs and hence their contribution to the dipole.

Absence of RFPs in the period 550 A.D.–1440 A.D. is related to the low geomagnetic power spectrum in spherical harmonics $n = 4–8$, which is associated with fewer data, resulting in a stronger effect of regularization. However, between 830 B.C. and 140 B.C. the absence of RFPs does not seem to be associated with low geomagnetic power spectrum, because the neighboring periods p1 and p3 (which have similar power spectra as period p2) contain RFPs. The absence of RFPs in this period could therefore genuinely reflect different field morphology and possibly different core dynamics activity in this time interval. The geomagnetic power spectrum for the recent period (p5) is much stronger than that of earlier periods because of the much better coverage and quality of the recent data.

Periods with lower values of geomagnetic power spectrum at high spherical harmonic degree lead to larger-scale field that mask small-scale field structures. Morphologically, it implies that two neighboring regions of opposite flux would be smoothed to one region of the more intense flux. This effect creates undulations in the magnetic equator and obscures RFPs, which limits relating RFPs to ADM changes. Perhaps surprisingly, the filtered models f8/11 and f5/11 show comparable number and more continuous RFPs than in the nonfiltered model. This may be associated to the resolution effects. Another possibility is that two neighboring RFPs, with low intensity values that do not pass the intensity criterion, may merge to one strong RFP after filtering and thus pass the intensity criterion. Note that the large interval of absence of RFPs (560 A.D.–1480 A.D.) in the nonfiltered model is occasionally abrupt in the filtered models f8/11 and f5/11. In these models spherical harmonic degrees 4 and 5 are not filtered whereas higher spherical harmonic degrees 9 and 10 are strongly reduced. Moreover, period p1 has the lowest values of spherical harmonic degrees 9 and 10. These results indicate that spherical harmonic degrees $n = 4–8$ strongly affect RFPs in the archeomagnetic field model. Indeed, the f3/8 filtered model strongly affects intermediate spherical harmonic degrees $n = 4–8$ and contains very few RFPs. Furthermore, period p4 had the lowest values of spherical harmonic degrees $n = 4–8$ compared to the other periods and in this period RFPs are absent (see Figure 5b).

Robust tracking results common to the nonfiltered as well as filtered models may shed light on the kinematics of RFPs. RFPs in all field models exhibit either a westward drift or to a much lesser extent quasi-stationary behavior. In most cases the RFPs drift to higher latitudes, thus systematically weakening the prevailing dipole polarity.

5. Conclusions

Our algorithm allows defining, identifying, and tracking reversed flux patches (RFPs). Our main findings are the following:

1. Most RFPs exhibit westward drift.
2. More than 75% of RFPs migrate toward higher latitudes.

©2015. American Geophysical Union. All Rights Reserved.

3. In some periods (but not all) the absence of RFPs is due to the low resolution of the field model. Overall, the data are not sufficient to show that the RFPs have not been present at all times in the recent few millennia.
4. Filtered models and comparison with GUFM1 suggest that RFPs are prominent.
5. Spherical harmonic degrees 4 and above strongly affect the existence of the RFPs.

Lastly, we draw attention to the need for new archeomagnetic data to allow for better constrained field models, as well as filters to better select the data used as database to the models. These new models will allow to better identify and track field structures (e.g., RFPs), and consequently to improve the understanding of RFPs and their role in core dynamics on millennial timescales.

Acknowledgments
The field model data for this paper are available at EarthRef.org Digital Archive (ERDA). Data set name: Global archeomagnetic field models CALS3k.4 and CALS3k.4b. Data set link: http://earthref.org/ERDA/1142/. F. Terra-Nova and G. A. Hartmann acknowledge grants 2013/14629-8 and 2010/10754-4, São Paulo Research Foundation (FAPESP), respectively. We would like to thank the Laboratoire de Planétologie et de Géodynamique (LPGNantes/CRNS) and the Instituto de Astronomia, Geofísica e Ciências Atmosféricas (IAG/USP) for the institutional support. This study was partially performed during a 4 month visit of F. Terra-Nova in LPGNantes. We are grateful to Richard Holme and Mathieu Dumberry for their constructive comments that significantly improved the manuscript.

References

Amit, H., and U. Christensen (2008), Accounting for magnetic diffusion in core flow inversions from geomagnetic secular variation, *Geophys. J. Int.*, *175*, 913–924.
Amit, H., and P. Olson (2006), Time-average and time-dependent parts of core flow, *Phys. Earth Planet. Inter.*, *155*, 120–139.
Amit, H., and P. Olson (2008), Geomagnetic dipole tilt changes induced by core flow, *Phys. Earth Planet. Inter.*, *166*, 226–238.
Amit, H., P. Olson, and U. Christensen (2007), Tests of core flow imaging methods with numerical dynamos, *Geophys. J. Int.*, *168*, 27–39.
Amit, H., J. Aubert, and G. Hulot (2010), Stationary, oscillating or drifting mantle-driven geomagnetic flux patches, *J. Geophys. Res.*, *115*, B07108, doi:10.1029/2009JB006542.
Amit, H., M. Korte, J. Aubert, C. Constable, and G. Hulot (2011), The time-dependence of intense archeomagnetic flux patches, *J. Geophys. Res*, *116*, B12106, doi:10.1029/2011JB008538.
Aubert, J. (2013), Flow throughout the Earth's core inverted from gomagnetic observations and numerical dynamo models, *Geophys. J. Int.*, *192*, 537–556, doi:10.1093/gji/ggs051.
Aubert, J., H. Amit, G. Hulot, and P. Olson (2008), Thermo-chemical flows couple the Earth's inner core growth to mantle heterogeneity, *Nature*, *454*, 758–761.
Aubert, J., C. Finlay, and F. Fournier (2013), Bottom-up control of geomagnetic secular variation by the Earth's inner core, *Nature*, *502*, 219–223, doi:10.1038/nature12574.
Aurnou, J., S. Andreadis, L. Zhu, and P. Olson (2003), Experiments on convection in Earth's core tangent cylinder, *Earth Planet. Sci. Lett.*, *212*, 119–134.
Bloxham, J. (1986), The expulsion of magnetic flux from the Earth's core, *Geophys. J. R. Astron. Soc.*, *87*, 669–678.
Bloxham, J., and D. Gubbins (1985), The secular variation of the Earth's magnetic field, *Nature*, *325*, 511–513.
Bloxham, J., and A. Jackson (1992), Time-dependent mapping of the magnetic field at the core-mantle boundary, *J. Geophys. Res*, *97*, 19,537–19,563.
Bullard, E. C., C. Freedman, H. Gellman, and J. Nixon (1950), The westward drift of the Earth's magnetic field, *Philos. Trans. R. Soc. London, Ser. A*, *243*, 67–92.
Busse, F. (1970), Thermal instabilities in rapidly rotating systems, *J. Fluid Mech.*, *44*, 441–460.
Chulliat, A., and N. Olsen (2010), Observation of magnetic diffusion in the Earth's outer core from Magsat, Ørsted and CHAMP data, *J. Geophys. Res.*, *115*, B05105, doi:10.1029/2009JB006994.
Dormy, E., J. Valet, and V. Courtillot (2000), Numerical models of the geodynamo and observational constrains, *Geochem. Geophys. Geosyst.*, *1*, 1037, doi:10.1029/2000GC000062.
Dumberry, M., and C. Finlay (2007), Eastward and westward drift of the Earth's magnetic field for the last three millennia, *Earth Planet. Sci. Lett.*, *254*, 146–157.
Finlay, C. (2008), Historical variation of the geomagnetic axial dipole, *Phys. Earth Planet. Inter.*, *170*, 1–14.
Finlay, C., and A. Jackson (2003), Equatorially dominated magnetic field change at the surface of Earth's core, *Science*, *300*, 2084–2086.
Gubbins, D. (1987), Mechanism for geomagnetic polarity reversals, *Nature*, *326*, 167–169.
Gubbins, D., A. Jones, and C. Finlay (2006), Fall in Earth's magnetic field is erratic, *Science*, *312*, 900–902.
Holme, R., and N. Olsen (2006), Core surface flow modelling from high-resolution secular variation, *Geophys. J. Int.*, *166*, 518–528.
Hulot, G., C. Eymin, B. Langlais, M. Mandea, and N. Olsen (2002), Small-scale structure of the geodynamo inferred from Ørsted and Magsat satellite data, *Nature*, *416*, 620–623.
Hulot, G., C. Finlay, C. Constable, N. Olsen, and M. Mandea (2010), The magnetic field of planet Earth, *Space Sci. Rev.*, *152*, 159–222, doi:10.1007/s11214-010-9644-0.
Jackson, A., A. Jonkers, and M. Walker (2000), Four centuries of geomagnetic secular variation from historical records, *Philos. Trans. R. Soc. London, Ser. A*, *358*, 957–990.
Jonkers, A., A. Jackson, and A. Murray (2003), Four centuries of geomagnetic data from historical records, *Rev. Geophys.*, *41*(2), 1006, doi:10.1029/2002RG000115.
Korte, M., and C. Constable (2011), Improving geomagnetic field reconstructions for 0–3 ka, *Phys. Earth Planet. Inter.*, *188*(3–4), 247–259.
Korte, M., and R. Holme (2010), On the persistence of geomagnetic flux lobes in global field models, *Phys. Earth Planet. Inter.*, *182*, 179–186.
Korte, M., F. Donadini, and C. Constable (2009), The geomagnetic field for 0–3 ka: 2. A new series of time-varying global models, *J. Geophys. Res.*, *10*, Q06008, doi:10.1029/2008GC002297.
Lowes, F. (1974), Spatial power spectrum of the main magnetic field, *Geophys. J. R. Astron. Soc.*, *36*, 717–730.
Moffatt, H. (1978), *Magnetic Field Generation in Electrically Conducting Fluids*, Cambridge Univ. Press, Cambridge, U. K.
Olsen, N., H. Luehr, T. J. Sabaka, I. Michaelis, J. Rauberg, and L. Tøffner-Clausen (2010), CHAOS-4—A high-resolution geomagnetic field model derived from low-altitude CHAMP data, Abstract GP21A–0992 presented at 2010 AGU Fall Meeting.
Olson, P., and H. Amit (2006), Changes in Earth's dipole, *Naturwissenschaften*, *93*, 519–542.
Olson, P., and U. Christensen (2002), The time averaged magnetic field in numerical dynamos with nonuniform boundary heat flow, *Geophys. J. Int.*, *151*, 809–823.
Olson, P., U. Christensen, and G. Glatzmaier (1999), Numerical modeling of the geodynamo: Mechanisms of field generation and equilibration, *J. Geophys. Res.*, *104*, 10,383–11,0404.

©2015. American Geophysical Union. All Rights Reserved.

Olson, P., I. Sumita, and J. Aurnou (2002), Diffusive magnetic images of upwelling patterns in the core, *J. Geophys. Res.*, *107*(B12), 2348, doi:10.1029/2001JB000384.

Wardinski, I., and M. Korte (2008), The evolution of the core-surface flow over the last seven thousands years, *J. Geophys. Res.*, *113*, B05101, doi:10.1029/2007JB005024.

Yukutake, T. (1967), The westward drift of the Earth's magnetic field in historic times, *J. Geomagn. Geoelec.*, *19*, 93–96.

©2015. American Geophysical Union. All Rights Reserved.

Appendix B

Algorithms

B.1 Magnetic equator finder

```
#include<stdio.h>
#include<math.h>
#include<stdlib.h>
#include<string.h>

//BC time frame
#define A 10 //maximum
#define B 1000 //minimum
#define C 10 //dt

//AD time frame
#define D 0 //maximum
#define E 1990 //minimum
#define F 10 //dt

float distance(float a, float b, float c, float d);

int main()
{
    int i, n, k, f, x, y, mark, cont;
    float x0, y0, y2, y3, distance0, distance1, lon, lat, intensidade;
    float mundo[400][200], equator1[400][5];
    FILE *entrada1;
    FILE *saida1;

    char nome1[100], nome2[100];
```

```
    /*
-------------------------------------------------------------------------------

    Matrix maker

-------------------------------------------------------------------------------
*/


for (i=A;i>=B;i=i-C){
    sprintf(nome1,"np_cmb_BC_%04d.dat",i);
    sprintf(nome2,"magnetic_equator_BC_%04d.dat",i);


            //fprintf(stdout,"file name: %s\n", nome1);

            entrada1 = fopen(nome1, "r");
            saida1 = fopen(nome2, "w");

            if (( entrada1, "r") == NULL ){
                    fprintf(stdout,"Sorry. It was impossible to find the
 data.");
                    exit(1);
            }

            //the sort of data
            n=3;

            while (n==3){
                    n = fscanf(entrada1,"%f %f %f", &lon, &lat, &
intensidade);
                    x = lon+180;
                    y = lat;
                    mundo[x][y]= intensidade;
    }

            /*
```

```
                finding a first point of the magnetic equator

-------------------------------------------------------------------------------

*/

                cont=0; //it will be sure the magnetic equator if there is
only one point in this longitude


                for(x=0;x<=360;x++){
                        for(y=180;y>=1;y--) //it is 1, because it does not
make sense to go futher than this
                        {
                                if(mundo[x][y]<0 && (mundo[x][y]*mundo[x][y
+1]<0)){
                                        y2=y;
                                        cont++;

                                }

                        }

                        if(cont==1){
                                x0=x;
                                k=x;
                                x=400;
                                y0=y2;
                                fprintf(saida1, "%f\t%f\n", x0-180 , y2);

                        }
                        cont=0;

                }

                /*
-------------------------------------------------------------------------------
```

```
                to search the equator line

-------------------------------------------------------------------------------

*/
                for(x=0;x<=400;x++) //putting 0 in the vector to sort the
troubled areas
                for(f=0;f<=5;f++)
                equator1[x][f] = -10;

                distance0=40;

                x=x0+1;
                //boundary conditions
                if(x==361)
                x=0;
                if(x==362)
                x=1;
                if(x==-1)
                x=360;
                if(x==-2)
                x=359;

                mark=0;//it says the direction it will search out the
magnetic equator

                n=0;
                while(n<=1500){
                        if(x!=k){
                                y3=0;
                                for(y=180;y>=1;y--) //it is 1, because it
does not make any sense to go futher than this
                                {
                                        if(mundo[x][y]*mundo[x][y-1]<0){
                                                if(y!=equator1[x][0] && y!=
equator1[x][1] && y!=equator1[x][2] && y!=equator1[x][3]){
                                                        y2=y;
                                                        distance1 = distance
```

```
(x0,y0,x,y2);
                                                    if(distance0 >=
distance1){
                                                        distance0 =
distance1;
                                                        y3=y2;
                                                    }
                                                }
                                            }
                                        }
                                        //printf("%d\t%d\t%f\t%f\n", n, x, y3,
equator1[x][1]); //it is a test print
                                        if(y3!=0){
                                            x0=x;
                                            y0=y3;
                                            if(equator1[x][0]==-10 && cont==0){
                                                equator1[x][0]=y0; //We save
 the first lap in here to be compared with the others
                                                cont=1;
                                            }
                                            if(equator1[x][0]!=-10 && equator1[x
][1]==-10 && cont==0){
                                                equator1[x][1]=y0; //We save
 the first lap in here to be compared with the others
                                                cont=1;
                                            }
                                            if(equator1[x][1]!=-10 && equator1[x
][2]==-10 && cont==0){
                                                equator1[x][2]=y0; //We save
 the first lap in here to be compared with the others
                                                cont=1;
                                            }
                                            if(equator1[x][2]!=-10 && cont==0){
                                                equator1[x][3]=y0; //We save
 the first lap in here to be compared with the others
                                            }

                                            fprintf(saida1, "%f\t%f\n", x0-180 ,
```

```
y0);
                distance0=40;

                if(mark==0)
                x++;
                if(mark==1)
                x--;
        }

        if(y3==0){
                switch(mark){
                        case 0:
                                mark=1;
                                x=x-1;
                        break;
                        case 1:
                                mark=0;
                                x=x+1;
                        break;
                }
        }
        n++;
        // boundary conditions
        if(x==361)
        {
        x=0;
        x0=0;
        }
        if(x==362)
        {
        x=1;
        x0=0;
        }
        if(x==-1)
        {
        x0=360;
        x=360;
        }
```

```
                                    if(x==-2)
                                    {
                                    x0=360;
                                    x=359;
                                    }
                                    cont=0;
                            }
                            if(x==k)
                            n=2000;
                    }

            }
return 0;
}


/*
    ------------------------------------------------------------------------------

    to calculate distance between two points on the grid
------------------------------------------------------------------------------
    */

float distance(float a, float b, float c, float d){

     return fabs(sqrt((a-c)*(a-c) + (b-d)*(b-d)));
     }
```

B.2 Magnetic hemisphere definer

```
#include<stdio.h>
#include<math.h>
#include<stdlib.h>
#include<string.h>

//BC time frame
#define A 10 //maximum
```

```
#define B 1000 //minimum
#define C 10 //dt

//AD time frame
#define D 0 //maximum
#define E 1990 //minimum
#define F 10 //dt

int main()
{
    int i, n, k, f, x, y, mark, cont, hemisphere;
    float x0, y0, y2, y3, distance0, distance1, lon, lat, intensidade;
    float mundo[400][200];
    FILE *entrada1;
    FILE *saida1;

    char nome1[100], nome2[100];

        /*
    ------------------------------------------------------------------------

        to make the matrix

    ------------------------------------------------------------------------
    */

    for (i=A;i>=B;i=i-C){
        sprintf(nome1,"magnetic_equator_BC_%04d.dat",i);
        sprintf(nome2,"magnetic_hemisphere_BC_%04d.dat",i);

                //fprintf(stdout,"file name: %s\n", nome1);

                entrada1 = fopen(nome1, "r");
                saida1 = fopen(nome2, "w");

                if (( entrada1, "r") == NULL ){
                        fprintf(stdout,"Sorry. It was impossible to find the
    data.");
```

```
                exit(1);
        }

        //putting zero in the whole world grid

        for(x=0;x<=360;x++)
        for(y=0;y<=180;y++)
        mundo[x][y] = 0;

        //sorting the data
        n=2;

        while (n==2){

                n = fscanf(entrada1,"%f %f", &lon, &lat);
                x = lon+180;
                y = lat;
                mundo[x][y]= 1;

        }

        for(x=0; x<=360;x++){
                mark=0;
                for(y=0; y<=180;y++){
                        if(mundo[x][y]==0 && mark==0)
                        {
                                lon=x;
                                lat=y;
                                hemisphere=0;
                                fprintf(saida1,"%d\t%f\t%f\n",
hemisphere, lon-180, lat);
                        }
                        if(mundo[x][y]==0 && mark==1)
                        {
                                lon=x;
                                lat=y;
                                hemisphere=1;
                                fprintf(saida1,"%d\t%f\t%f\n",
```

```
    hemisphere, lon-180, lat);
                                }
                                if(mundo[x][y]!=0 && mark==0)
                                {
                                        lon=x;
                                        lat=y;
                                        hemisphere=0;
                                        fprintf(saida1,"%d\t%f\t%f\n",
    hemisphere, lon-180, lat);
                                        mark=1; //the next step would be in
    southern hemisphere
                                        cont=1; //it is just to skip the
    next if
                                }
                                if(mundo[x][y]!=0 && mark==1 && cont==0)
                                {
                                        lon=x;
                                        lat=y;
                                        hemisphere=0;
                                        fprintf(saida1,"%d\t%f\t%f\n",
    hemisphere, lon-180, lat);
                                        mark=0;
                                }
                                cont=0;
                        }
                }

        }

return 0;
}
```

B.3 Polarity assigner

```
#include<stdio.h>
#include<math.h>
#include<stdlib.h>
```

```
#include<string.h>

//BC time frame
#define A 10 //maximum
#define B 1000 //minimum
#define C 10 //dt

//AD time frame
#define D 0 //maximum
#define E 1990 //minimum
#define F 10 //dt

int main()
{
    int i, n, x, y, hemisphere;
    float x0, y0, y2, y3, distance0, lon2, lon, lat, intensity, intensity0;
    float mundo[400][200];
    FILE *entrada1;
    FILE *entrada2;
    FILE *saida1;

    char nome1[100], nome2[100], nome3[100];
/*
    ------------------------------------------------------------------------

      to make the vector
------------------------------------------------------------------------
   */

    for (i=A;i>=B;i=i-C){
        sprintf(nome1,"magnetic_hemisphere_BC_%04d.dat",i);
                sprintf(nome3,"np_cmb_BC_%04d.dat",i);
                sprintf(nome2,"reversal_regions_BC_%04d.dat",i);

        //fprintf(stdout,"file name: %s\n", nome1);

                entrada1 = fopen(nome1, "r");
                entrada2 = fopen(nome3, "r");
```

```
                saida1 = fopen(nome2, "w");
                if (( entrada1, "r") == NULL ){
                        fprintf(stdout,"Sorry. It was impossible to find the
    data.");
                        exit(1);
                }

                //sorting the data
                n=3;

                while (n==3){
                        n = fscanf(entrada1,"%d %f %f", &hemisphere, &lon2,
    &lat);
                        x = lon2+180;
                        y = lat;
                        mundo[x][y]= hemisphere;
                }

/*
    ------------------------------------------------------------------------

     Starting to search the regions of reversal field
    ------------------------------------------------------------------------
    */
                n=3;
                intensity0 = 0.0;
                while (n==3){
                        n = fscanf(entrada2,"%f %f %f", &lon, &lat, &
    intensity);
                        x = lon+180;
                        y = lat;
                        if ( (intensity < 0 && mundo[x][y] == 1) || (
    intensity > 0 && mundo[x][y] == 0))
                        fprintf(saida1, "%f\t%f\t%f\n", lon, lat, intensity)
    ;
                        else
                        fprintf(saida1, "%f\t%f\t%f\n", lon, lat, intensity0
    );
```

```
                }
    }

        return 0;
}
```

B.4 Reversed flux patch center finder

```
#include<stdio.h>
#include<math.h>
#include<stdlib.h>
#include<string.h>

//BC time frame
#define A 10 //maximum
#define B 1000 //minimum
#define C 10 //dt

//AD time frame
#define D 0 //maximum
#define E 1990 //minimum
#define F 10 //dt

int main ()
{
        float intensidade, lon, lat, intensidade2, lon2, lat2;
        int n, cont, i, x, y, g, h, l, k;
        double mundo[600][400];
        char nome1[100], nome2[100], nome3[100];
        FILE *entrada1;
        FILE *entrada2;
        FILE *saida1;

        for (i=D;i<=E;i=i+F)
        {
                sprintf(nome1,"np_f8_cmb_%04d.dat",i);
                sprintf(nome2,"f8_reversal_regions_%04d.dat",i);
```

```
            sprintf(nome3,"i_f8_reversal_center_%04d.dat", i);
            //fprintf(stdout,"file name: %s\n", nome1);


            entrada1 = fopen(nome1, "r");
            entrada2 = fopen(nome2, "r");
            saida1 = fopen(nome3, "w");

            if (( entrada1, "r") == NULL )
            {
                    fprintf(stdout,"Sorry, file cannot be open.");
                    exit(1);
            }
            //fprintf(stdout,"walk here, place one");
            //converting list in matrix
            n=3;
            while (n==3)
            {
                    n = fscanf(entrada1,"%f %f %f", &lon, &lat, &
intensidade);
                    // converting float (lon and lat) in int
                    x = lon+180;
                    y = lat;
                    mundo[x][y]= intensidade;
            }

            //reading the regions of reversed flux
            n=3;
            while (n==3)
            {
            n = fscanf(entrada2,"%f %f %f", &lon2, &lat2, &intensidade2)
;

                    if(intensidade2 != 0)
                    {       //fprintf(stdout,"walk here, place two");
                            x = lon2+180;
                            y = lat2;
                            //variables for boundary condition
```

```
g=x-1;
h=y-1;
k=x+1;
l=y+1;
//boundary conditions
if(y==180)
l=0;
if(y==0)
h=180;
if(x==360)
k=0;
if(x==0)
g=360;

//is it maximum? It is answered here.
if( mundo[x][y]- mundo[g][h] >0)
if( mundo[x][y]- mundo[g][y] >0)
if( mundo[x][y]- mundo[g][l] >0)
if( mundo[x][y]- mundo[x][h] >0)
if( mundo[x][y]- mundo[x][l] >0)
if( mundo[x][y]- mundo[k][h] >0)
if( mundo[x][y]- mundo[k][y] >0)
if( mundo[x][y]- mundo[k][l] >0)
{
        fprintf(saida1,"%d\t%d\t%f\n", x
-180, y, intensidade2);
        fprintf(stdout,"%d\t%d\t%d\t\n", i,
x-180, y); //when it is BC years use -i instead i
}

//is it minimum? It is answered here.
if( mundo[x][y]- mundo[g][h] <0)
if( mundo[x][y]- mundo[g][y] <0)
if( mundo[x][y]- mundo[g][l] <0)
if( mundo[x][y]- mundo[x][h] <0)
if( mundo[x][y]- mundo[x][l] <0)
if( mundo[x][y]- mundo[k][h] <0)
if( mundo[x][y]- mundo[k][y] <0)
```

```
                                if( mundo[x][y]- mundo[k][l] <0)
                                {
                                        fprintf(saida1,"%d\t%d\t%f\n", x
    -180, y, intensidade2);
                                        fprintf(stdout,"%d\t%d\t%d\t\n", i,
    x-180, y); //when it is BC years use -i instead i
                                }
                        }
                }
        }
        return 0;
```

B.5 Reversed flux patch tracker

```
#include<stdio.h>
#include<math.h>
#include<stdlib.h>
#include<string.h>

#define PI 3.14159265

//BC time frame
#define A 10 //maximum
#define B 1000 //minimum
#define C 10 //dt

//AD time frame
#define D 0 //maximum
#define E 1990 //minimum
#define F 10 //dt


float distance_esferica(int a, int b, int c, int d);
int main(){

        int fois, cont, i, a, x, y, x1, y1;
        float lon, lat, distance, distance0;
```

```
int patches0[400][200], patches1[400][200];
FILE *entrada1;
char nome1[100], nome2[100];

fois=0; //it says that this is the first interaction
//putting zero in the initial matrix
for(x=0; x<=360;x++)
for(y=0; y<=180;y++)
patches0[x][y]=0;
//putting zero in all over the second matrix
for(x=0; x<=360;x++)
for(y=0; y<=180;y++)
patches1[x][y]=0;
//inicial values
distance0=700;
cont=0;

for (i=A;i>=B;i=i-C){
        sprintf(nome1,"f8_reversal_center_BC_%04d.dat",i);

        //fprintf(stdout,"file name: %s\n", nome1);



        entrada1 = fopen(nome1, "r");

        if (( entrada1, "r") == NULL )
        {
                fprintf(stdout,"Sorry, the file cannot be open.");
                exit(1);
        }




        //iteraction matrix 1
        if(fois==0){
                while ((fscanf(entrada1,"%f %f",&lon, &lat))==2)
```

```
                        {
                                // changing float (lon and lat) into int
                                x = lon+180;
                                y = lat;
                                cont++;
                                patches0[x][y]= cont;
                                fprintf(stdout,"%d\t%d\t%d\t%d\n", patches0[
x][y], -i, x-180, y);
                        }

                }

                if(fois==1){

                        while ((fscanf(entrada1,"%f %f", &lon, &lat))==2)
                        {
                                // changing float (lon and lat) into int

                                x = lon+180;
                                y = lat;
                                patches1[x][y]= -1;
                        }

                        for(x=0; x<=360;x++){
                                for(y=0; y<=180;y++){
                                        if(patches0[x][y]>0){
                                                for(x1=0; x1<=360;x1++){
                                                        for(y1=0; y1<=180;y1
++){
                                                                if(patches1[
x1][y1]==-1){

distance = distance_esferica(x, y, x1 , y1);
                                                                        //
fprintf(stdout,"%d\t%f\n", -i, distance); //test print
                                                                        if(
distance < distance0){
```

```
                patches1[x1][y1]=patches0[x][y];

                distance0 = distance;
                                                                        }
                                                                    }
                                                                }
                                                            }
                                                            distance0=700;
                                                        }
                                                    }
                                                }

                                                for(x1=0; x1<=360;x1++){
                                                    for(y1=0; y1<=180;y1++){
                                                        if(patches1[x1][y1]==-1){
                                                            cont++;
                                                            patches1[x1][y1]=cont;
                                                        }

                                                    }
                                                }
                                                //changing initial matrix and printing
                                                for(x=0; x<=360;x++)
                                                for(y=0; y<=180;y++){
                                                    patches0[x][y]=patches1[x][y];
                                                    if(patches0[x][y] != 0)
                                                    fprintf(stdout,"%d\t%d\t%d\t%d\n", patches0[
x][y], -i, x-180, y);
                                                }
                                                //putting zeros in the second matrix
                                                for(x=0; x<=360;x++)
                                                for(y=0; y<=180;y++)
                                                patches1[x][y]=0;

                                                //initial values
                                                distance0=700;
                                            }
                                            fois=1;
```

```
        }

        for (i=D;i<=E;i=i+F){
                sprintf(nome1,"f8_reversal_center_%04d.dat",i);

                //fprintf(stdout,"file name: %s\n", nome1);



                entrada1 = fopen(nome1, "r");

                if (( entrada1, "r") == NULL )
                {
                        fprintf(stdout,"Sorry, but the file cannot be open."
);
                        exit(1);
                }

                if(fois==1){

                        while ((fscanf(entrada1,"%f %f", &lon, &lat))==2)
                        {
                                // changing float (lon and lat) into int

                                x = lon+180;
                                y = lat;
                                patches1[x][y]= -1;
                        }

                        for(x=0; x<=360;x++){
                                for(y=0; y<=180;y++){
                                        if(patches0[x][y]>0){
                                                for(x1=0; x1<=360;x1++){
                                                        for(y1=0; y1<=180;y1
++){
                                                                if(patches1[
x1][y1]==-1){
```

```
distance = distance_esferica(x, y, x1 , y1);
                                                                    //
fprintf(stdout,"%d\t%f\n", i, distance); //test print
                                                                    if(
distance < distance0){

        patches1[x1][y1]=patches0[x][y];

        distance0 = distance;
                                                                    }
                                                                }
                                                            }
                                                        }
                                                        distance0=700;
                                                    }
                                                }
                                            }

                                            for(x1=0; x1<=360;x1++){
                                                for(y1=0; y1<=180;y1++){
                                                    if(patches1[x1][y1]==-1){
                                                        cont++;
                                                        patches1[x1][y1]=cont;
                                                    }

                                                }
                                            }
                                            //changing initial matrix and printing
                                            for(x=0; x<=360;x++)
                                            for(y=0; y<=180;y++){
                                                patches0[x][y]=patches1[x][y];
                                                if(patches0[x][y] != 0)
                                                fprintf(stdout,"%d\t%d\t%d\t%d\n", patches0[
x][y], i, x-180, y);
                                            }
                                            //putting zeros in the second matrix
                                            for(x=0; x<=360;x++)
                                            for(y=0; y<=180;y++)
```

```
                        patches1[x][y]=0;

                        //initial values
                        distance0=700;



                }
                fois=1;
        }

return 0;
}

float distance_esferica(int a, int b, int c, int d){

        float distance, P1, b1, d1;
        int P;

        P = a - c;
        P1= P*0.0174532;
        b1= b*0.0174532;
        d1= d*0.0174532;
        distance = cos(b1)*cos(d1) + sin(b1)*sin(d1)*cos(P1);
        //fprintf(stdout,"1\t%d\t%f\n", P, distance); //test print
        distance = acos(distance)*3449.2;
        //fprintf(stdout,"2\t%d\t%f\n", P, distance); //test print
        return distance;
}
```